








A role for the thalamus in danger evoked awakening during sleep

Received: 14 August 2024

Accepted: 15 July 2025

Published online: 31 July 2025

 Check for updates

Ida Luisa Boccalaro^{1,2,5}, Mattia Aime ^{1,2}, Florence Marcelle Aellen^{1,3}, Thomas Rusterholz^{1,2}, Micaela Borsa ^{1,2}, Ivan Bozic ^{1,2}, Andrea Sattin ⁴, Tommaso Fellin ⁴, Carolina Gutierrez Herrera^{1,2}, Athina Tzovara ^{1,3} & Antoine Adamantidis ^{1,2} ✉

Sleep involves a relative disconnection from the environment, yet sensory stimuli can still trigger awakenings. The mechanism underlying sensory vigilance and stimulus discrimination during sleep remains unclear. Here, we showed that neutral auditory stimuli evoked responses across parallel auditory and non-auditory pathways, including the auditory cortex and thalamus, the hippocampus and centro-medial thalamus (CMT). Using a convolutional neural network, we identified CMT activity as the most discriminant hub for auditory-evoked sleep-to-wake transitions among all recorded structures. Furthermore, we found that prior associative learning of auditory cues with danger (conditioned stimulus, CS+) resulted in increased awakening upon CS+ exposure during NREM, but not REM, sleep. These sleep-to-wake transitions were blocked by optogenetic silencing of CMT neurons during CS+ exposure in sleeping mice. Altogether, these results suggest a central role of the CMT neurons in the residual processing of behaviorally-relevant information in the sleeping brain functioning as one of the major hubs for awakening in response to danger.

The sleeping brain maintains a residual ability to respond to external sensory information despite reduced responsiveness to the environment^{1,2}. Accordingly, auditory-evoked responses persist in thalamo-cortical circuits during NREM^{3–5} and REM sleep⁶, supporting cognitive processes such as word-pair learning and semantic discrimination^{7–9}.

During wakefulness, auditory information follows a well-defined pathway, propagating from the inferior colliculus to the medial geniculate nucleus (MG) of the thalamus, and then reaching the auditory cortex, where it is processed for perception and higher-order interpretation¹⁰. Evidence suggests that this pathway remains active during sleep, with auditory-evoked responses persisting in the auditory thalamus^{5,11} and auditory cortex^{7,12,13}, although with state-dependent modulation.

In sleep, auditory processing is more complex, as the brain must not only encode sensory input but also determine whether to trigger an awakening. This decision-making process involves additional circuits, including brainstem arousal centers such as the locus coeruleus (LC)¹⁴ and the mesencephalic tegmentum¹⁵ as well as the mediodorsal thalamus, which integrates sensory and arousal signals^{15–17}. Sleep-to-wake transitions depend not only on sensory input but also on brain state, ongoing activity, oscillatory dynamics, and auditory cue saliency^{2,3,14,18–20}. This selective vigilance is critical for survival, allowing awakening to personally relevant auditory stimuli, such as a baby's cry or one's name^{21–24}. Auditory fear conditioning studies indicate that the discrimination of danger-associated stimuli relies on subcortical circuits, with the medial sector of the auditory thalamus (ATm), including the posterior intralaminar nucleus (PIN), relaying auditory signals from

¹Zentrum für Experimentelle Neurologie, Department of Neurology, Inselspital University Hospital Bern, University of Bern, Bern, Switzerland. ²Department of Biomedical Research, University of Bern, Bern, Switzerland. ³Institute of Computer Science, University of Bern, Bern, Switzerland. ⁴Optical Approaches to Brain Function Laboratory, Istituto Italiano di Tecnologia, Genova, Italy. ⁵Present address: Beth Israel Deaconess Medical Center, Harvard Medical School, Boston, MA, USA. ✉e-mail: antoine.adamantidis@unibe.ch

the inferior colliculus directly to the amygdala^{11,25}. This subcortical pathway bypasses the auditory cortex, enabling rapid defensive responses to salient auditory cues.

Yet, the brain mechanisms underlying the discrimination of auditory cues with content-relevant information—e.g., danger versus safety—during sleep remain unclear. Here, we investigated the brain and behavioral responses of sleeping mice subjected to re-exposure to danger or neutral auditory cues and identified the brain-wide mechanisms responsible for sensory integration during sleep.

Results

Hierarchy of brain responses to auditory stimuli across sleep–wake states

We first recorded neural responses evoked by neutral auditory stimuli across sleep–wake states in freely-moving mice. Chronic multi-site single-unit and local field potential (LFP) electrodes were stereotactically implanted in the primary auditory cortex (Au1) and the dorsal medial geniculate (dMG) nucleus of the auditory thalamus together with electroencephalogram/electromyogram (EEG/EMG) electrodes (see “Methods,” Fig. 1a). Additional electrodes were implanted in the hippocampus (HP) and in the central medial thalamus (CMT), as these structures are either not associated with the processing of auditory stimuli or regulate fear during wakefulness and sleep–wake transitions, respectively^{16,17,26–32}. After habituation to the recording conditions, neural and LFP responses to auditory stimuli in these structures were recorded across wakefulness, NREM, and REM sleep (100 ms duration; 1, 2.5, and 5 kHz frequency randomly delivered at 30, 55, and 80 dB over an hour, see “Methods”; Fig. 1a).

To test the implication of CMT neurons in auditory-evoked awakenings in a data-driven approach, we trained a convolutional neural network (CNN) using LFP recordings to identify which brain structure showed the highest discriminative activity between auditory-evoked NREM sleep-to-wake transitions (^ΔNREMs-WAKE, Fig. 1b) as compared to those that did not wake the animals up (^ΔNREMs-NREMs, Fig. 1b). After training, the network reached a mean AUC score of 0.82 ± 0.01 on the trained recordings, 0.81 ± 0.01 on the validation sets, and 0.81 ± 0.02 on the test experimental sets, indicating robust differences in local neuronal activity between ^ΔNREMs-NREMs vs ^ΔNREMs-WAKE transitions at single-trial level (see “Methods”; Supplementary Table 1e and Table 1). For both ^ΔNREMs-NREMs and ^ΔNREMs-WAKE transitions, the sigma-filtered CMT recorded LFPs showed the highest saliency as compared to other recorded sites, including cortical frontal (F) and parietal (P) EEGs (Fig. 1c in 9–16 Hz, Supplementary Fig. 1a in 1–20 Hz and, Supplementary Fig. 1b in 10–40 Hz, respectively). Consistent with this result, we found that CMT showed an activation profile that significantly differed between ^ΔNREMs-NREMs vs ^ΔNREMs-WAKE transitions upon auditory stimuli, while all other structures tested had similar profiles (Fig. 1d), identifying the CMT nucleus as the most discriminant structure in determining awakening upon auditory stimuli.

We further trained the neural network on baseline recordings (i.e., in the absence of auditory stimuli) as a control condition to predict spontaneous NREMs-WAKE vs NREMs-NREMs transitions (Supplementary Fig. 1c). Artificial sham stimuli were used for trial extraction, network training (see “Methods”), and control analysis. The performances of the baseline network on the training, validation, and test sets were 0.90 ± 0.01 (training), 0.73 ± 0.06 (validation), and 0.73 ± 0.05 (test), respectively (Supplementary Table 1a). This was significantly lower (*t*-test, *t* = 3.25, *p* < 0.05) in comparison to the training with auditory stimulations, where performances were 0.80 ± 0.01 (training), 0.80 ± 0.02 (validation), and 0.79 ± 0.01 (test). The AUC score for the baseline recording was particularly low for the majority of folds, whereas the AUC scores for the stimulation case were elevated (always >0.75) and consistent across folds (Supplementary Table 1a), further confirming the prediction that CMT neurons contribute to auditory stimuli-evoked arousals. CNN trained on

electrophysiological recordings filtered in the slow wave range (0.5–4 Hz) suggested a predominant drive by CMT, but also dMG and frontal EEG as compared to Au1 and parietal EEG (Supplementary Fig. 1d). Consistent with the CNN model, we found that spindle rate showed a significant increase in CMT during ^ΔNREMs-NREMs as compared to ^ΔNREMs-WAKE transitions, and, to a lesser extent in other recorded structures (HP, dMG) except for the Au1 cortex (Fig. 1e). Note that similar observations were made for spindles detected from frontal and parietal EEG electrodes (Fig. 1e). Accordingly, the probability of ^ΔNREMs-WAKE transitions was significantly higher when auditory stimuli were phase-locked to the UP phase of local CMT slow waves (Fig. 1f), presumably because of CMT neuron hyper-excitability¹⁶. In contrast, this effect was not significant for other recorded sites (HP, dMG) while it was opposite for Au1 (DOWN phase) when neurons are in a low-excitability state (Fig. 1f). While we cannot fully discern ongoing slow waves from auditory-evoked slow waves due to the prominent influence of auditory stimuli on all electrophysiological recordings, the observed region-specific differences in polarity, particularly the pronounced thalamic modulation of the UP state in the CMT, is consistent with evoked responses and k-complex-related activity reported previously^{33–35}.

Animals showed a rapid habituation to auditory stimulations (Fig. 2a–d) and each of these reliably evoked local field potentials (LFPs) and single-unit responses (Fig. 2e, and f, g, respectively) from all recorded sites and stimuli (Supplementary Fig. 2, Supplementary Fig. 3, Supplementary Fig. 5, Supplementary Fig. 5, Supplementary Fig. 6). Auditory-evoked LFP responses in all regions of interest exhibited short latencies (<50 ms) during wakefulness, NREM, and REM sleep (Supplementary Fig. 2b). Interestingly, high amplitude potentials and increased spiking activities were recorded from CMT in responses to auditory stimuli as compared to those recorded in HP and dMG in particular during NREM sleep, even if not significantly (Supplementary Fig. 2b, c). Note the reverse polarity in Au1 LFPs accompanied by a decrease in spiking rate in response to auditory stimuli during NREM. Importantly, the spiking rate of CMT neurons was significantly higher for auditory stimuli that evoked ^ΔNREMs-WAKE as compared to ^ΔNREMs-NREMs (Fig. 2h). This was specific to CMT neuron activities as evoked LFPs and spiking rates recorded from other structures remained unchanged during ^ΔNREMs-WAKE or ^ΔNREMs-NREMs transitions (Fig. 2i–k), confirming the CNN analysis in identifying the CMT nucleus as the most critical structure in triggering awakening in response to auditory stimuli.

Silencing of CMT neurons blocks auditory-evoked awakening

To assess the role of CMT neurons in mediating auditory-evoked awakenings during sleep, adeno-associated viruses (AAV) AAV5-CamKII-ArchT3.0-eYFP or AAV2-CamKII-eYFP (control) were stereotactically injected into the CMT area before animals were chronically implanted with multi-site tetrodes in the Au1, dMG, CMT, and HP, an optical fiber above the CMT, cortical EEG and EMG electrodes (see “Methods,” Fig. 3a). After habituation to the experimental conditions, we observed that optogenetic silencing of ArchT-expressing CMT neurons during auditory stimulations (Fig. 3b–d, Supplementary Fig. 7a–c) significantly decreased the probability of auditory-evoked ^ΔNREMs-WAKE transitions, but had no effect on awakenings from REM sleep (Fig. 3e, Supplementary Fig. 7d). The short silencing of CMT neurons itself had no effects on awakenings during baseline recordings (Supplementary Fig. 7d, No Audio Stim Laser ON). Strikingly, auditory stimuli significantly decreased the global number of slow waves during NREM sleep in all recorded structures except the HP, an effect that was blocked by the optogenetic silencing of ArchT-expressing CMT neurons (Supplementary Fig. 7e). Note that spindle rates (Supplementary Fig. 7f) and sleep architecture (Supplementary Fig. 7g) remained unchanged upon optogenetic manipulations. These results indicated that CMT neurons promote sensory-driven arousal.

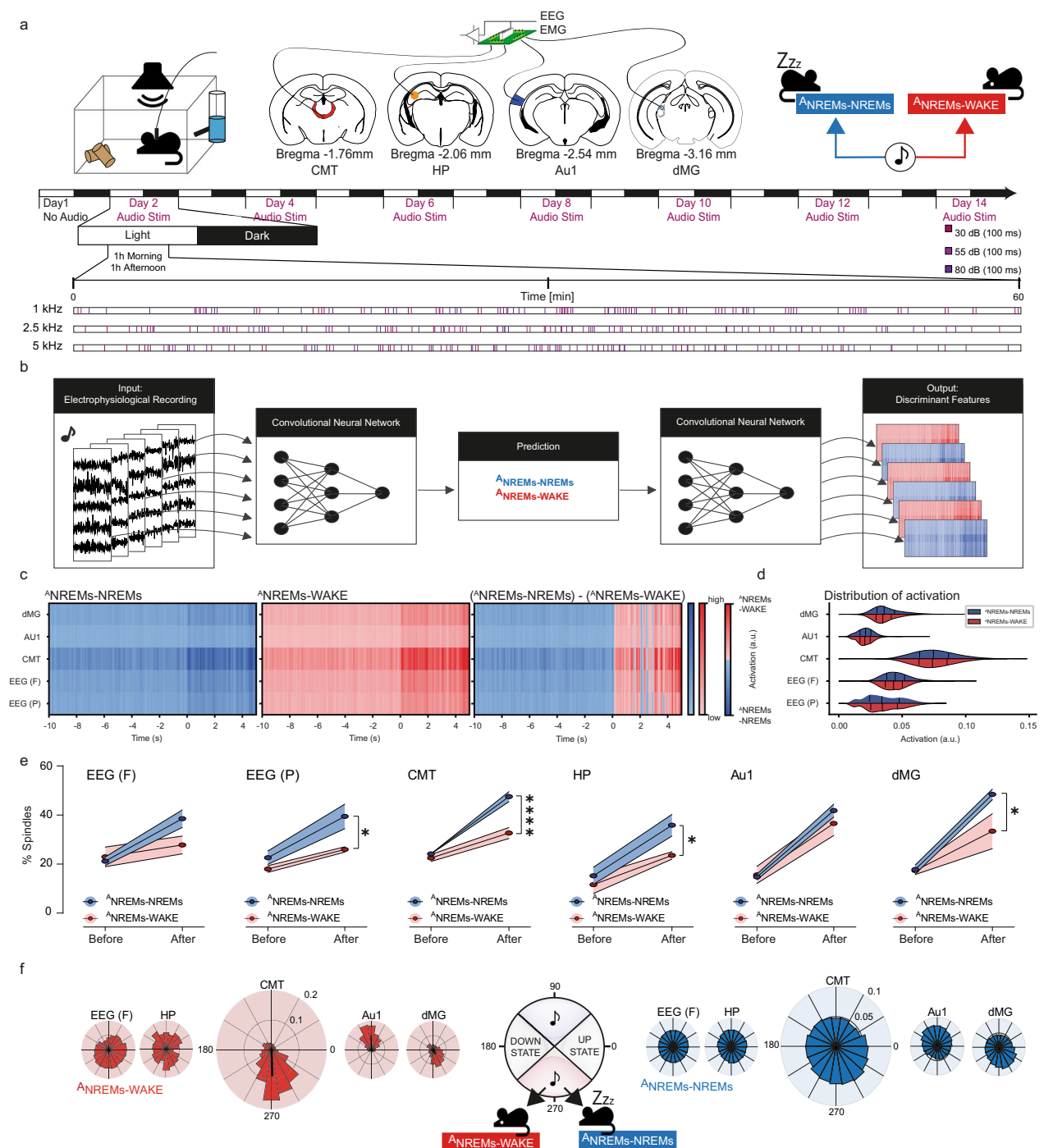


Fig. 1 | Local CMT oscillations predict Δ NREMs-to-WAKE. **a** Experimental setup: multi-site tetrode implanted in the central medial thalamus (CMT), hippocampus (HP), primary auditory cortex (Au1), and dorsal medial geniculate (dMG), together with EEG/EMG electrodes. Experimental timeline included recording of 1-h session (360 pure tones randomly distributed) twice a day during wake, NREMs, and REMs (n = 14 sessions). The first day was recorded without auditory stimulation as a baseline (Day 1—No Audio). For the remaining 14 days, recordings were made only on alternate days when auditory stimulation was applied, resulting in 7 days of recorded data with auditory stimulation. **b** Modeling pipeline used to train the Convolutional Neural Network (CNN) and extract discriminant features. The training was done with a ten-fold cross-validation, on LFP and EEG traces filtered in the sigma band (from 9 to 16 Hz) and extracted from -10 to 5 s relative to the sound's onset. **c** Mean activation maps, quantifying the relevance of individual LFP/EEG traces across time for the network's classification of whether a given trial was Δ NREMs-NREMs (in blue, left) vs Δ NREMs-WAKE (in red, middle) conditions. Right: the difference between the mean activation maps of the Δ NREMs-WAKE (n = 546 trials) and Δ NREMs-NREMs (n = 1055

trials) conditions. **d** Distribution of the mean network activation across trials per region. **e** Percentage of spindle rate recorded during Δ NREMs-NREMs (in blue) and Δ NREMs-WAKE transitions (in red), for frontal (p = 0.0754, t = 2.256, df = 16) and parietal EEGs (p = 0.0113, t = 3.191, df = 16), CMT (p < 0.0001, t = 6.095, df = 16), HP (p = 0.0449, t = 2.520, df = 16), Au1 (p = 0.4945, t = 1.097, df = 16) and dMG (p = 0.0315, t = 2.697, df = 16). **f** Circular plot of the phase-locking of EEG slow waves (SWs) recorded from EEG, HP, CMT, Au1, and dMG to Δ NREMs-to-WAKE (red, n = 247 SWs from N = 5 mice) and Δ NREMs-NREMs (blue, n = 9397 SWs from N = 5 mice) transitions. Data were analyzed using two-way ANOVA followed by Šidák's multiple comparisons test (two-sided). Exact p-values, t-values, and degrees of freedom are reported. Data are presented as mean \pm S.E.M.; individual data points are overlaid, and error bars represent the SEM. Source data are provided as a Source Data file. © 2025 Allen Institute for Brain Science. Allen Mouse Brain Atlas. Available from: <https://atlas.brain-map.org/>. a was modified from Gent et al., Nat. Neurosci. 21, 10.1038/s41593-018-0164-7 (2018), with permission from Springer Nature.

Table 1 | Additional evaluation metrics for the trained networks presented in the main manuscript

| | Train set | Validation set | Test set |
|-----------|-------------|----------------|-------------|
| Precision | 0.75 ± 0.07 | 0.74 ± 0.07 | 0.73 ± 0.08 |
| Recall | 0.67 ± 0.09 | 0.65 ± 0.08 | 0.64 ± 0.09 |
| F1-score | 0.70 ± 0.03 | 0.68 ± 0.03 | 0.67 ± 0.04 |

Here we additionally report the precision, recall, and the F1-score for the train, validation, and test sets (mean ± standard deviation).

Danger-encoding cues elicit arousal during NREM, but not REM, sleep

We next tested whether CMT neurons also contribute to processing behaviorally relevant stimuli associated with danger during sleep by triggering awakening. Chronic multi-site single-unit and local field potential (LFP) electrodes were stereotactically implanted in the CMT region, together with cortical EEG and EMG electrodes (Fig. 4a). After recovery and habituation to the recording conditions, mice were trained to discriminate between a conditioned stimulus (CS+, 5 kHz) paired with mild electric foot shock and a neutral auditory stimulus (CS−, 1 kHz; see “Methods”; Fig. 4a). Mice showed no preference for either of the CS+ or CS− during habituation (Day 1) and progressively developed a significant increase of freezing behavior in response to CS+, but not CS− (Day 2, see “Methods”; Fig. 4a, b). After conditioning, animals returned to their home cage, where they were allowed to sleep. Before conditioning, the percentage of awakenings for CS− vs CS+ stimuli was similar (Fig. 4c, Supplementary Fig. 8, a “Hab”), however, after conditioning CS+ stimuli alone (i.e., without shocks) induced a significant increase of ^ΔNREMs-WAKE transitions as compared to CS− stimuli (Fig. 4c, Supplementary Fig. 8, a “Rec”).

Importantly, the spiking rate of CMT neurons was significantly higher during CS+-evoked ^ΔNREMs-WAKE transitions as compared to ^ΔNREMs-NREMs transitions (Fig. 4d). In addition, CMT neurons exhibited a significant decrease in bursting activity upon CS+-evoked ^ΔNREMs-WAKE transitions (post-tone) during the recall sessions as compared to their activity during spontaneous (pre-tone) ^ΔNREMs-WAKE (“CS+ Rec” in Fig. 4e) but not in ^ΔNREMs-NREM transitions (Fig. 4f). This contrasts with their stable bursting activity in all other conditions (Fig. 4e, f and Supplementary Fig. 8b) and suggests that tonic activity of CMT neurons upon CS+ exposure induces arousal¹⁶ and supports sensory integration³⁶.

To test whether this switch from bursting to tonic spiking activity after fear conditioning is also associated with a reorganization of network activity during danger vs neutral cue discrimination, we longitudinally recorded the activity of single CMT neurons across the behavioral conditioning and cues exposure during post-sleep using two-photon calcium imaging in head-restrained sleeping mice. AAV1-CaMKII-GCaMP8m was stereotactically infused into the CMT area before EEG/EMG electrodes and an aberration-corrected endoscope lens³⁷ were chronically implanted (see “Methods”; Fig. 5a). After habituation to the recording conditions, we longitudinally recorded the response of GCaMP8-expressing CMT neuron populations to CS− and CS+ during wakefulness and NREM sleep immediately after Habituation (Day 1) and Recall (Day 3) (see “Methods”; Fig. 5b). Consistent with previous findings, all animals that successfully learned the task exhibited increased freezing to the CS+ during the Recall session (Fig. 5c) and stable CS-evoked calcium transients across the behavioral task and sleep-wake states (Fig. 5d, e). Yet, the correlation of CS− vs CS+ evoked responses of the CMT neuron population during NREM sleep decreased following “Recall” as compared to “Habituation” session, while it remained stable when the animals were awake (Fig. 5f, g). As previously observed, animals showed an increase of ^ΔNREMs-WAKE upon CS+, as compared to CS−, exposure during NREM sleep after

acquisition of the fear conditioning task (Fig. 5h, Supplementary Fig. 8c). Consistently, the activity of CMT neurons was significantly higher for CS+-evoked ^ΔNREMs-WAKE as compared to ^ΔNREMs-NREMs transitions after conditioning, while no difference was observed during Habituation (Fig. 5i). Note that this analysis was restricted to the CS+, as CS− elicited awakening episodes were almost negligible after conditioning. Altogether, these results suggested that the CMT neuronal network undergoes a spatial reorganization, selectively during NREM sleep, in response to danger-encoding vs neutral cues (as represented in Fig. 5j).

Finally, we tested the contribution of CMT neurons to the discrimination of danger vs neutral cues during NREM sleep. Animals were stereotactically injected with AAV5-CamKII-ArchT-eYFP or AAV2-CamKII-eYFP (control) into the CMT area and chronically implanted with optic fibers above the CMT, and EEG/EMG electrodes (see “Methods”; Fig. 6a). All animals showed similar performance in discriminating CS− from CS+ stimuli after conditioning (Fig. 6b). Consistent with previous findings, we observed that optogenetic silencing of ArchT3.0-expressing CMT neurons during NREM sleep blocked CS+-evoked ^ΔNREMs-WAKE transitions in ArchT but not in control (eYFP) animals, as revealed by their significant decrease in CS+-evoked ^ΔNREMs-WAKE transitions in Recall as compared to controls (Fig. 6c, Supplementary Fig. 9a). None of the optogenetic manipulation affected the sleep-wake architecture (Fig. 6d, f, Supplementary Fig. 9b, c, e, f). Consistent with our results, no behavioral differences were observed when CMT neurons were optogenetically silenced during REM sleep (Fig. 6e, Supplementary Fig. 9d). These results suggested that CMT neuronal activity contributes to the awakening induced by the perception of danger during NREM, but not REM, sleep.

Discussion

Sleep is a state associated with low awareness, or responsiveness, to environmental stimuli in the animal kingdom. It has adapted its architecture, timing, and habitat relative to the perceived risk of perturbation or danger, including temperature, light, noise, wind, or predation^{38–40}. This state of apparent vulnerability is compensated by a fluctuating threshold of sensory disconnection^{2,41,42} and regular awakenings, as for instance sentinels in gregarious species. Adaptive responses during sleep are likely to engage mechanisms in the central nervous system capable of detecting environmental threats based on various sensory modalities^{20,21,43}. Our results revealed that centro-medial thalamic neurons play an important role in evoking sensory-driven awakening from NREM sleep consistent with its role in arousal^{14–16,26,44,45}. Although auditory stimuli during sleep primarily trigger the classical auditory pathway^{7,11,12,46}, parallel circuits are activated and include the locus coeruleus¹⁴, hippocampus¹³, and medio-dorsal thalamus¹⁵ through mechanisms that remain to be determined.

Prediction from a CNN model and experimental validation expands previous findings on the role of spindles in protecting sleep to local CMT spindles in auditory-evoked awakening from NREM sleep. Indeed, our results further show that local spindles, particularly those originating in the CMT region, provide sensory protection during NREM sleep, in line with previous studies showing that spindles regulate sleep stability and modulate sensory responsiveness^{18,19}. Consistent with its role in arousal from NREM sleep during spontaneous sleep¹⁶, decoding analysis and optogenetic silencing revealed that sensory stimuli selectively recruit CMT neurons during sleep as a possible mechanism for integrating environment stimuli during sleep. This further reflects the central role of the thalamic neurons in stress or fear reaction^{26,29}, sensory encoding¹⁵ and working memory^{30,47,48} during wakefulness.

During sleep, the switch of CMT neuron activity from a burst to a tonic discharge mode appears as a selective response to environmental danger, consistent with a role in the “Wakeup call” hypothesis³⁶. Spiking patterns in thalamic neurons influence the type of information

that is relayed to the cortex. For instance, bursting discharge enhances stimulus detection in the visual cortex, whereas tonic firing supports accurate, linear processing⁴⁹. Recordings from mediodorsal thalamic (MD) neurons in mice reveal that their firing mode is crucial for fear extinction, as mutant mice with enhanced burst firing show impaired extinction, whereas tonic-evoking microstimulation rescues this deficit, highlighting the MD's role in modulating fear responses³². During

NREM sleep, auditory tone induced a higher occurrence of bursts in the auditory thalamus⁵ or cortex¹². Before associative learning, we observed post-tone bursts of activity in CMT neurons during NREM sleep, hypothetically associated with sleep stability¹⁶. However, after learning, CMT neurons shifted their pattern of discharge to a tonic firing upon CS+ exposure, consistent with an arousal trigger¹⁶, and possibly supporting a more complex emotional response such as fear

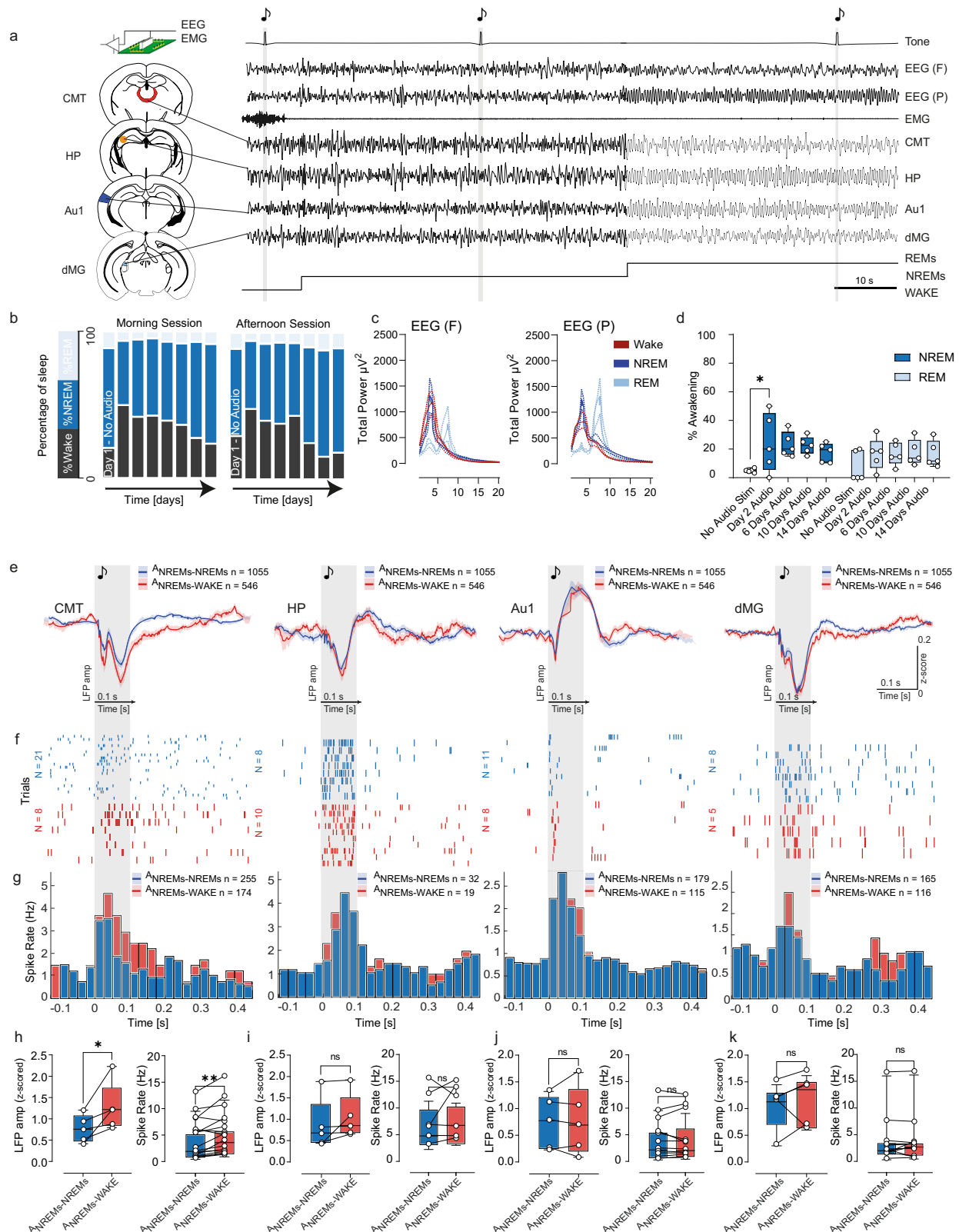


Fig. 2 | Auditory-evoked responses in non-sensory CMT during Δ NREMs-to-WAKE transitions. **a** Experimental setup involved implanting multi-site tetrodes in the central medial thalamus (CMT), hippocampus (HP), primary auditory cortex (Au1), and dorsal medial geniculate (dMG), along with EEG/EMG electrodes. Right: representative traces from all implanted electrodes. **b** Percentage of total duration of wake, NREMs, and REMs of the first day without auditory stimulations and the subsequent 14 sessions. **c** Frontal and parietal EEG power spectra analysis for wake, NREM, and REM sleep. **d** Percentage of awakenings from NREMs (light blue) and REMs (dark blue) across baseline (No Audio Stim) and 14 days of auditory stimulation ($n = 14$ sessions from $N = 5$ mice). Two-way ANOVA with Šidák's multiple comparisons (two-sided): significant difference for NREM, 1st Day vs No Audio Stim ($p = 0.0477$, $t = 2.980$, $df = 40$). **e** Average LFP responses to 80 dB 5 kHz tones (in gray) during NREMs recorded from CMT, HP, Au1, and dMG. Auditory-evoked LFPs in which the animals continue to sleep (Δ NREMs-NREMs) are in blue ($n = 1055$ stimuli from $N = 5$ mice), others when the animals wake up (Δ NREMs-WAKE) in red ($n = 546$ stimuli from $N = 5$ mice). **f** Representative single-unit auditory-evoked responses of CMT, HP, Au1, and dMG during Δ NREMs-NREMs (blue) or Δ NREMs-WAKE (red). **g** Averaged peristimulus histogram (PSTH) of recorded units (CMT

$n = 17$; HP $n = 6$; Au1 $n = 12$; dMG $n = 12$) during Δ NREMs-NREMs (blue, CMT $n = 255$; HP $n = 32$; Au1 $n = 179$; dMG $n = 165$ stimuli) or Δ NREMs-WAKE (red, CMT $n = 174$; HP $n = 19$; Au1 $n = 115$; dMG $n = 116$ stimuli) from $N = 5$ mice. **h–k** Quantification of auditory-evoked LFP peak amplitude (left) and spike rate (right) during Δ NREMs-NREMs (blue) versus Δ NREMs-WAKE (red). Two-sided paired t-tests for (**h**) CMT: LFP $p = 0.0464$, $t = 2.851$, $df = 4$; spike rate $p = 0.0039$, $t = -3.37$, $df = 16$. **i** HP: LFP $p = 0.1972$, $t = 1.545$, $df = 4$; spike rate $p = 0.4493$, $t = -0.82$, $df = 5$. **j** Au1: LFP $p = 0.8069$, $t = 0.2611$, $df = 4$; spike rate $p = 0.8576$, $t = 0.18$, $df = 11$. **k** dMG: LFP $p = 0.5483$, $t = 0.6548$, $df = 4$; spike rate $p = 0.5835$, $t = 0.56$, $df = 11$. Data were analyzed using two-way ANOVA followed by Šidák's multiple comparisons test (two-sided) and two-sided paired t-tests where applicable. Exact p-values, t-values, and degrees of freedom are reported. Box plots show the median (center line), 25th–75th percentiles (box), and minimum/maximum values (whiskers); individual data points are overlaid. Data are presented as mean \pm S.E.M.; individual data points are overlaid. Source data are provided as a Source Data file. © 2025 Allen Institute for Brain Science. Allen Mouse Brain Atlas. Available from: <https://atlas.brain-map.org/>. **a** was modified from Gent et al., Nat. Neurosci. 21, 10.1038/s41593-018-0164-7 (2018), with permission from Springer Nature.

or danger. Furthermore, two-photon experiments showed a spatial reorganization of calcium responses in CMT neurons during NREM sleep after fear conditioning that correspond to the changes of neuronal firing patterns observed in electrophysiology experiments. Overall, these findings emphasize the centro-medial thalamus's pivotal function in integrating sensory information and orchestrating appropriate responses to environmental cues, ensuring both sleep protection and effective arousal when necessary.

While our study highlights the pivotal role of the centro-medial thalamus (CMT) in danger-evoked awakening during sleep, one limitation of our approach is that optogenetic silencing may have partially affected adjacent thalamic regions; while the viral expression and fiber placement were centered in the CMT, some off-target effects cannot be fully excluded. Previous lesion studies implicated subcortical circuits, including the auditory thalamus and its projections to the amygdala, in the discrimination of danger-associated stimuli^{11,25}. Accordingly, the CMT lies at the intersection of arousal and sensory pathways as it receives strong input from the amygdala and other subcortical structures, and relays this information to cortical regions including the prefrontal cortex, where it potentially contributes to higher-order arousal and sensory integration^{50,51}. In this study, the absence of sensory-evoked awakenings during REM sleep reflects the higher sensory threshold during that state in humans and animals, presumably as a protective mechanism against disruptive environmental stimuli⁵². In addition, the restorative functions of REM sleep are seen as prerequisites for effective waking function with brief awakenings from REM sleep preparing the organism for immediate fight or flight^{43,53}, as compared to awakenings from NREM sleep. Our results showed that awakenings with sham stimulations are similar ($\pm 20\%$) for both NREM and REM sleep. However, stimuli previously paired with mild electric foot shocks significantly increase awakenings during NREM sleep (30–60%), indicating a fear response that was not observed during REM sleep, where awakenings remain at $\pm 20\%$ regardless of previous fear association. Opto-silencing of CMT neurons specifically altered the percentage of awakening from NREM sleep, while it decreased awakenings for CS+ and increasing awakenings for CS− after conditioning. This suggested that discrimination occurs during NREM sleep. Together with previous research^{20,22,23,41,43,52–55}, our study further supports the idea that a residual vigilance remains during NREM sleep possibly for monitoring the environment for potential threats, while REM sleep represents a disconnected state.

Our study expands the integrative role of the CMT neurons between subcortical nuclei, including the amygdala, and the neocortex, as previously suggested^{50,51,56}. Together with their role in processing other sensory modalities during sleep (e.g., olfaction⁵⁷),

our findings suggest a “sentinel” role for CMT neurons that integrate behaviorally relevant subcortical and cortical inputs during sleep^{14,58,59}. Collectively, our results advocate for a residual processing of sensory information during NREM sleep and expand the repertoire of brain mechanisms at play during sleep, such as uni-hemispheric sleep in marine mammals⁶⁰, sleep while flying in birds⁶¹, or visual scanning in gulls⁶² that optimize sleep over behavioral trade-offs to surrounding threats. These open new avenues to further understand how information is integrated during sleep, using mice as a simplified model for studying sensory processing and consciousness in both healthy and diseased states.

Methods

Animals

All experimental procedures, including animal handling, surgery, and experiments followed the Canton Bern Swiss Veterinary Office guidelines (license n. BE 129/2020). Adult male C57Bl6 mice from Janvier Labs (FR), 8–12 weeks old at the time of the surgery were used for in vivo electrophysiological, optogenetic, and behavioral experiments. Mice were single-housed in Plexiglas cages at constant temperature (20–23 °C), humidity (40–60%), and circadian cycle (12-h light/dark cycle, starting at 08:00 a.m.). Food and water were available ad libitum. After surgery, mice underwent a recovery period with 3 days of subcutaneous administration of analgesic (Metacam). On the 6th day, they were chronically tethered to recording cables (and optic fibers, respectively); the experiment started just after 10 days to let the mice recover from the surgery and habituate to the experimental conditions.

Viral injections

Six-week-old mice were anesthetized with isoflurane (5% for induction, 1.25–1.75% for maintenance) in oxygen and placed on a stereotaxic frame (Model 940, David Kopf Instruments). Before all surgical procedures, saline and Metacam were administered subcutaneously to provide hydration and analgesia. After shaving, a midline incision along the skull was made to expose the surface, ensuring proper positioning by aligning the Bregma and Lambda lines (around 4.6 mm caudally). Under microscopic control, a craniotomy was performed using a surgical drill.

Injections were carried out using a Hamilton syringe (7000 series, model 7000.5, 0.5 μ L volume) mounted on a programmable syringe pump (Pump 11 Elite Nanomite Infusion/Withdrawal Programmable Syringe Pump, Harvard Apparatus). The viruses used were: AAV5-CamKII-ArchT for the optogenetics experimental groups, AAV2-CamKII-eYFP for the optogenetics control groups, and AAV1-CaMKII-GCaMP8m for imaging experiments.

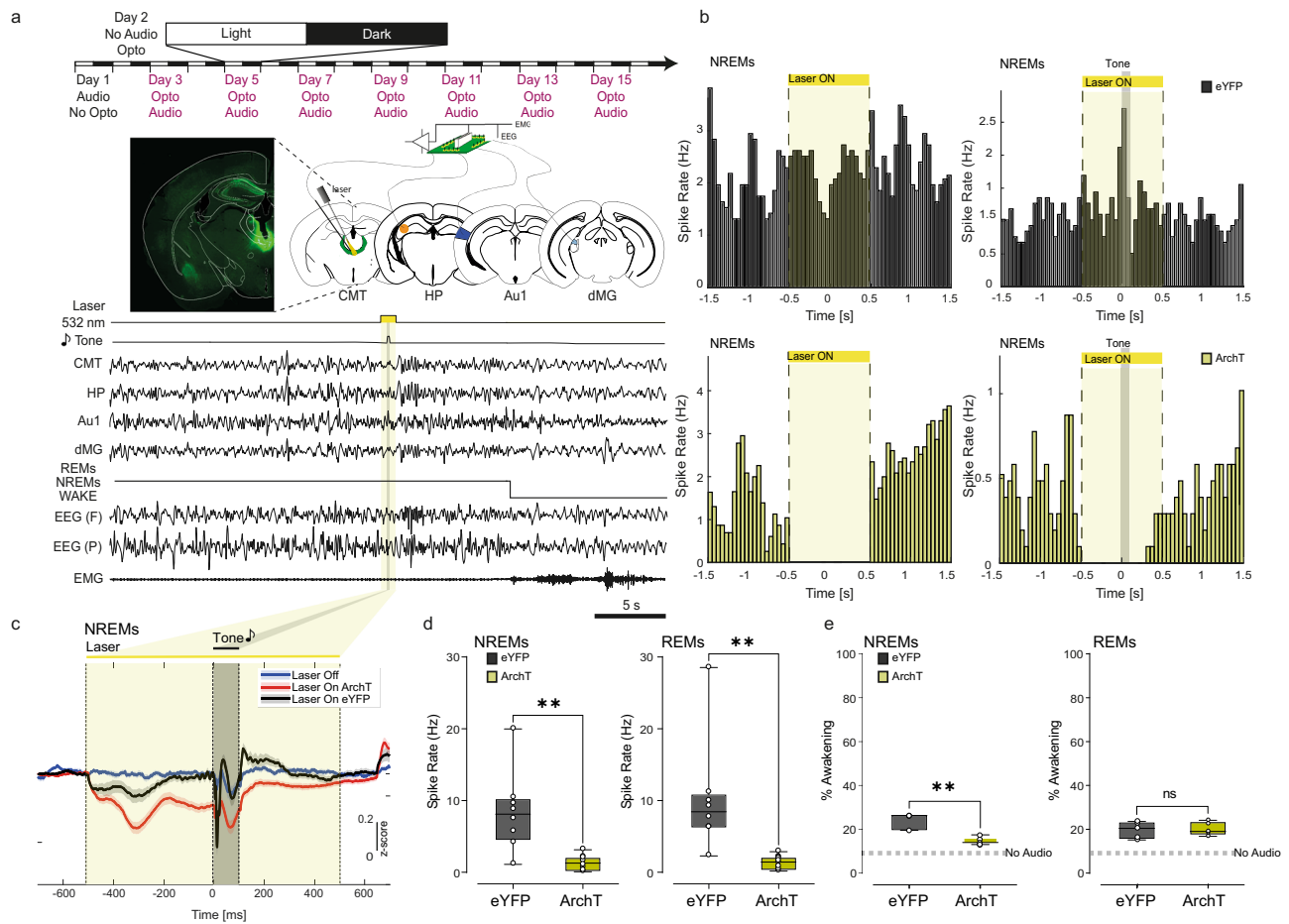


Fig. 3 | Optogenetic silencing of CMT neurons blocks Δ NREMs-to-WAKE transitions. **a** Experimental timeline and setup showing multi-site tetrodes implanted in CMT, HP, Au1, dMG, together with EEG, and EMG electrodes. Bottom: Representative traces from the different regions and the corresponding hypnogram with EEG/EMG data. As shown in yellow, the laser was ON from 0.5 s before to 0.5 s after stimulus onset (Laser, in yellow and Tone, in gray). **b** Representative spike rate of eYFP- (top in black) and ArchT- (bottom in yellow) expressing CMT neurons upon optogenetic silencing without (left) or with (right) auditory stimulation (top left black, n = 90 trials; top right black, n = 100 trials, and bottom left yellow, n = 12 trials; bottom right yellow, n = 39 trials, respectively). **c** Average event-related LFP recorded in CMT in response to the auditory stimuli (Tone, in gray) and to optogenetic silencing (in yellow) without optical stimulation (Laser OFF, blue trace; N = 10 mice), with optogenetic silencing in ArchT mice (Laser ON, red trace; N = 5) and eYFP mice (Laser ON, black trace; N = 5 mice). **d** Auditory-evoked spike rate recorded from CMT neurons upon optogenetic silencing during NREMs (left) and REMs (right) in ArchT (n = 10 units from N = 5 mice, average of 110 trials) and eYFP

mice (n = 8 units from N = 5 mice, average of 112 trials). Two-sided unpaired t-tests: NREM: p = 0.0011, t = 3.985, df = 16; REM: p = 0.0028, t = 3.531, df = 16. **e** Percentage of awakening from NREMs (left) and REMs (right) in ArchT (n = 7028 during NREM; n = 730 during REM from N = 5 mice) and eYFP mice (n = 6429 during NREM; n = 553 during REM from N = 5 mice). Dotted lines (No Audio) represent the percentage of awakening measured in the absence of auditory stimulation for both groups, serving as a control baseline. Two-sided unpaired t-tests: NREM: p = 0.0012, t = 4.876, df = 8; REM: p = 0.7981, t = 0.2644, df = 8. Data were analyzed using two-sided unpaired t-tests. Exact p-values, t-values, and degrees of freedom are reported. Box plots show the median (center line), 25th–75th percentiles (box), and minimum/maximum values (whiskers); individual data points are overlaid. Data are presented as mean \pm S.E.M. Source data are provided as a Source Data file. © 2025 Allen Institute for Brain Science. Allen Mouse Brain Atlas. Available from: <https://atlas.brain-map.org/>. **a** was modified from Gent et al., Nat. Neurosci. 21, 10.1038/s41593-018-0164-7 (2018), with permission from Springer Nature.

Each virus was injected into the central medial thalamus (CMT) at coordinates 1.58 mm anterior-posterior (AP), 0.75 mm medial-lateral (ML), and 4.1 mm dorsal-ventral (DV) at a 10° angle, based on Paxinos' and Franklin's mouse brain atlas. The injection volume was 200 nL delivered at a rate of 50 nL/min. To ensure optimal viral diffusion, the needle was kept in place for at least 10 min post-injection before being slowly withdrawn. All plasmids were obtained from the University of Zurich Viral Vector Facility, ensuring high-quality viral preparations optimized for specific neuronal targeting and expression.

AAV5-CamKII-ArchT. This viral vector was used for optogenetics experiments to achieve cell-specific expression of ArchT (archaerhodopsin), a light-activated proton pump, under the control of the CamKII promoter to target excitatory neurons.

AAV2-CamKII-eYFP. This control vector was used in optogenetics experiments to express enhanced yellow fluorescent protein (eYFP) under the CamKII promoter, serving as a fluorescence-based control.

AAV1-CaMKII-GCaMP8m. This vector was used for imaging experiments, expressing GCaMP8m, a genetically encoded calcium indicator, under the CamKII promoter for monitoring neuronal activity in excitatory neurons.

Tetrode implantation

Electrodes used for EEG and grounding signals were made of stainless-steel screws, for EMG signals instead were used bare-ended steel wires. Tetrodes were obtained with four strands of 10- μ m tungsten wire (CFW0010954, California Fine Wire), which were twisted and connected to an electrode interface board by gold pins (EIB-36-PTB,

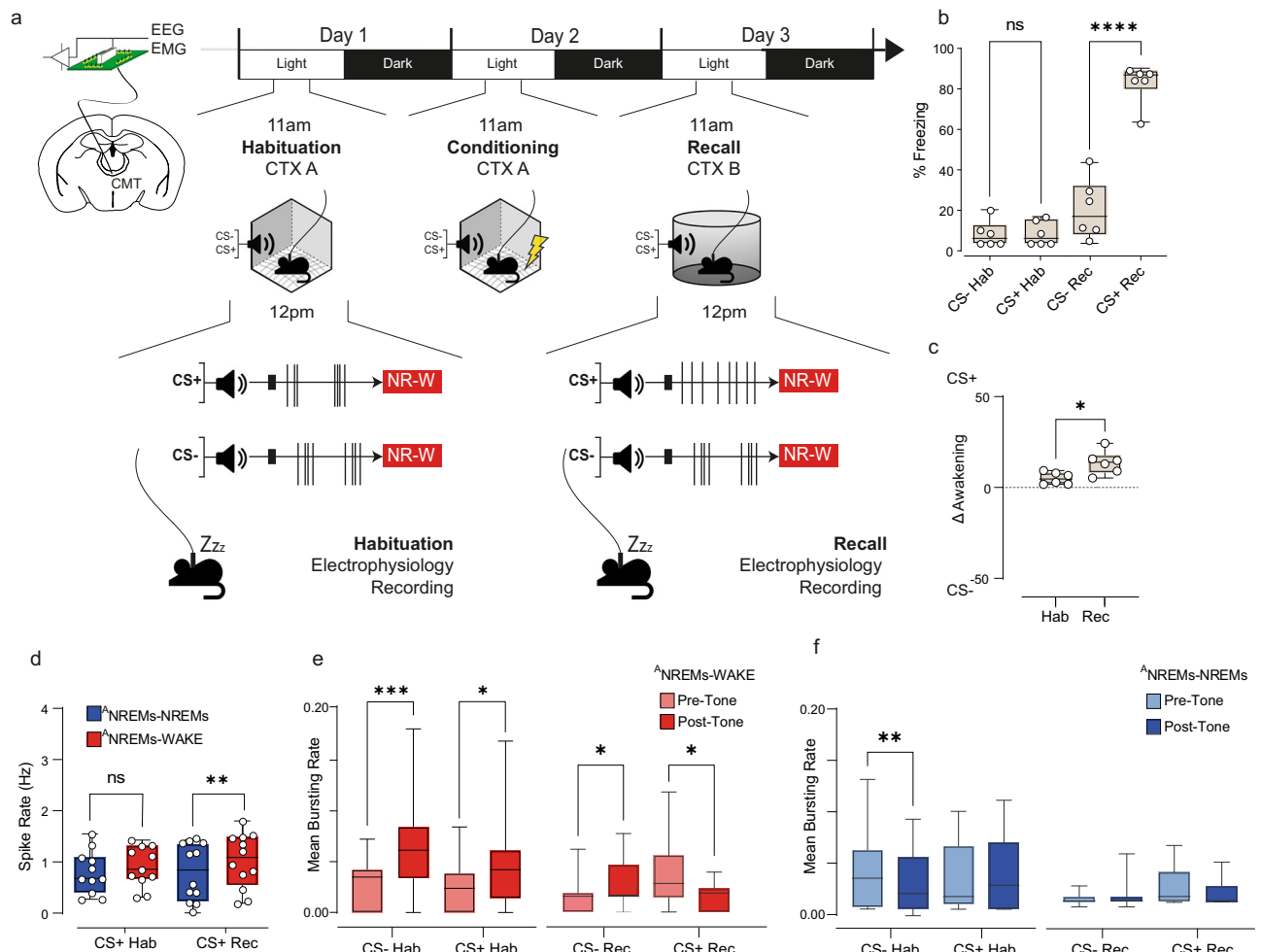


Fig. 4 | CMT neurons modulate safety vs danger perception during NREMs.

a Experimental timeframe of fear conditioning and electrophysiological recordings. **b** Percentage of behavioral freezing upon CS- and CS+ exposure during Habituation (p = 0.9986, t = 0.048, df = 20) and Recall (p < 0.0001, t = 10.98, df = 20) sessions (N = 6 mice). **c** Percentage of awakening between the CS- and CS+; Delta values are calculated as the difference between [percentage of awakening for CS+] - [percentage of awakening for CS-] during Habituation (Hab, p = 0.2164, t = 1.649, df = 20) and Recall (Rec, p = 0.0195, t = 2.855, df = 20) sessions (N = 6 mice). **d** Average spike rate of CMT neurons upon CS+ exposure during Habituation (n = 11 units from N = 6 mice, p = 0.2476, t = 1.565, df = 21) and Recall (n = 13 units from N = 6 mice, p = 0.0041, t = 3.512, df = 21) sessions. **e** Mean bursting rate of CMT neurons upon CS- and CS+ exposure in Habituation (n = 11 units from N = 6 mice, CS- p = 0.0003, t = 4.603, df = 15; CS+ p = 0.0146, t = 2.720, df = 17) and Recall (n = 13 units from N = 6 mice, CS- p = 0.0413, t = 2.197, df = 18; CS+ p = 0.0290, t = 2.454, df = 13) sessions for ^ΔNREMs-WAKE transitions for spontaneous (Pre-tone,

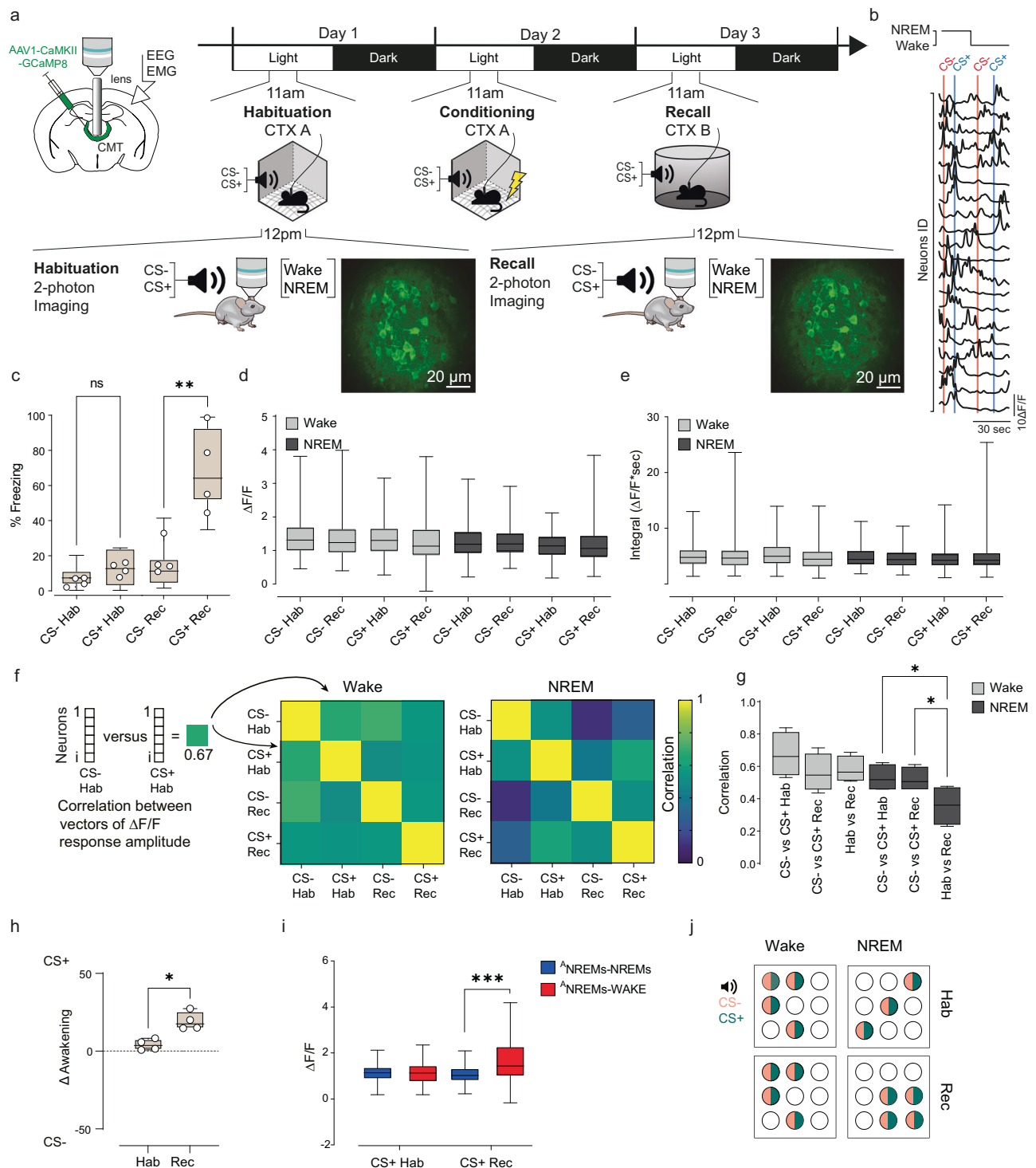
light red) versus evoked (Post-tone, dark red) burst activity. **f** Mean bursting rate of CMT neurons upon CS- and CS+ exposure during Habituation (n = 11 units from N = 6 mice, CS- p = 0.0011, t = 4.013, df = 15; CS+ p = 0.4237, t = 0.819, df = 17) and Recall (n = 13 units from N = 6 mice, CS- p = 0.1897, t = 1.363, df = 18; CS+ p = 0.2918, t = 1.120, df = 9) sessions for ^ΔNREMs-NREMs transitions for spontaneous (Pre-tone, in light blue) vs evoked (Post-tone, in dark blue) burst activity. Data were analyzed using two-way ANOVA with Šidák's multiple comparisons test for (**b-d**), and two-sided paired t-tests for (**e, f**). Exact p-values, t-values, and degrees of freedom are reported. Box plots show the median (center line), 25th–75th percentiles (box), and minimum/maximum values (whiskers); individual data points are overlaid. Data are presented as mean ± S.E.M. Source data are provided as a Source Data file. © 2025 Allen Institute for Brain Science. Allen Mouse Brain Atlas. Available from: <https://atlas.brain-map.org/>. a was modified from Gent et al., Nat. Neurosci. 21, 10.1038/s41593-018-0164-7 (2018), with permission from Springer Nature.

Neuralynx). One tetrode (so four electrodes) was implanted per region of interest. Anesthesia was induced using isoflurane in oxygen and maintained using a mix of medetomidine (0.27 mg/kg), midazolam (5 mg/kg), and fentanyl (0.05 mg/kg). As described above, the animals were placed on the stereotaxic frame, and the holes for the position of the electrodes were drilled. The preparation consisted of the implantation of two EEGs, one placed in the skull above the frontal lobe and one above the parietal lobe; the ground screw was placed above the cerebellum, and the two EMG wires were sutured to the trapezoid muscle. Tetrodes were implanted unilaterally in CMT (1.58 AP, 0.75 ML, 4.1 DV, 10° angle), HP (2.2 AP, 1.5 ML, 1.9 DV), Au1 (2.6 AP, 4.5 ML, 2 DV), and dMG (3.2 AP, 2.2 ML, 3.7 DV). For optogenetic experiments, an optic fiber of 200 μm diameter was additionally implanted in CMT via attachment to the respective tetrode in ArchT and eYFP mice. Once the

electrodes were fixed by applying Tetric EvoFlow cement by Ivoclar Vivadent, the EEGs (frontal, parietal, and the ground) and the EMG wires were connected to the interface board. To finalize the surgery, Paladur methacrylate cement was applied to fix the implant and protect the skull surface. Anesthesia was terminated by injecting Atipamezole, Naloxone, and Flumazenil subcutaneously.

Endoscope implantation

For CMT 2-photon imaging experiments, 6-week-old male mice were anesthetized with an intraperitoneal (i.p.) injection of a mix containing medetomidine (0.27 mg kg⁻¹), midazolam (5 mg kg⁻¹), and fentanyl (0.05 mg kg⁻¹) in sterile NaCl 0.9% (MMF-mix). Analgesia was achieved by local application of 100 μl of lidocaine (lurocaine, 1%) and subcutaneous (s.c.) injection of metacam



(meloxicam, 5 mg kg⁻¹). 40 μl of dexamethasone (Methameson, 0.1 mg ml⁻¹) was administered intramuscularly (i.m.) in the quadriceps to prevent inflammation potentially caused by the friction of the drilling. A heating pad was positioned underneath the animal to keep the body temperature at 37 °C. Eye dehydration was prevented by topical application of eye ointment. The skin above the skull was disinfected with modified ethanol 70% and betadine before an incision was made. An 800-μm-diameter craniotomy was drilled above the CMT. A small track was made with a 0.7 mm sterile needle through the tissue (down to 2.8 mm from the brain surface) to aid endoscope insertion. A custom 500-μm-diameter aberration-corrected microendoscope (type II)³⁷ was

slowly inserted (rate: 1 μm/s) above the CMT, as previously described⁶³. Custom microendoscopes were based on a GRIN rod and a corrective polymer lens providing an enlarged field-of-view (FOV) and more homogeneous spatial resolution across the FOV, compared to uncorrected endoscopes³⁷. The implant was cemented to the skull with dental acrylic and dental cement. For polysomnographic recordings, three EEG electrodes made of stainless-steel screws were placed in the skull to record EEG signals (screw #1: AP: +2.5 ML: ±3.0 mm; screw #2: AP: -2.3 mm, ML ±2.0 mm; reference screw: AP: -4.3 mm, ML +0.5 mm) and two EMG bare-ended wires were sutured to the trapezius muscle of the neck to record muscle activity signals.

Fig. 5 | Single-cell and population activity of CMT neurons across fear conditioning and sleep. **a** Schematic of the experimental procedure. (Bottom) Expression profile of GCaMP8-expressing CMT neurons. **b** Representative $\Delta F/F$ activity profiles of a population of CMT neurons in response to CS- and CS+ stimulations during wakefulness and NREM sleep. **c** Freezing percentage upon CS- and CS+ presentation during Habituation and Recall ($N = 4$ mice; one-way ANOVA, $F(7, 21) = 0.6765$, CS- vs CS+ Hb $p = 0.5219$; CS- vs CS+ Rec $p = 0.0057$). **d** Mean CS- and CS+ evoked $\Delta F/F$ activity profiles during wakefulness (light gray) or NREM sleep (dark gray) after Habituation or Recall test ($n = 89$ neurons from $N = 4$ mice). **e** Quantification of average integral values ($\Delta F/F$'s) in response to CS- or CS+ during wakefulness (light gray) or NREM sleep (dark gray) after Habituation or Recall test ($n = 89$ neurons from $N = 4$ mice). **f** Left: Representative correlation between vectors of $\Delta F/F$ response amplitudes; Color-coded population matrices of correlation coefficients upon CS- and CS+ presentation after Habituation or Recall test in wakefulness (middle) or NREM sleep (right). **g** Quantification of correlation coefficients represented in (f) ($n = 89$ neurons from $N = 4$ mice; one-way ANOVA, $F(3, 15) = 38.45$; CS-vsCS+Hab vs HabvsRec $p = 0.02$; CS-vsCS+Rec vs HabvsRec

$p = 0.04$). **h** Percentage of awakening between the CS- and CS+: Delta values are calculated as the difference between [percentage of awakening for CS+] - [percentage of awakening for CS-] during Habituation and Recall sessions ($N = 4$ mice; paired t-test $p = 0.0451$, $t = 3.319$, $df = 3$). **i** Average CS+ evoked $\Delta F/F$ activity profiles during awakening from NREM sleep (red) or maintained sleep (blue) after Habituation or Recall test ($n = 89$ neurons from $N = 4$ mice; one-way ANOVA, $F(3, 211) = 8.869$; $p = 0.000015$). **j** Graphical representation of CMT neurons spatial reorganization after Recall test, selectively during NREM sleep. Circles represent neurons; filled circles represent selectivity to CS- (light red) or CS+ (light green), respectively. Data were analyzed using one-way or two-way ANOVA with Tukey post hoc test or two-sided paired t-tests, as appropriate. Exact p-values and degrees of freedom are reported. Box plots show the median (center line), 25th–75th percentiles (box), and minimum/maximum values (whiskers); individual data points are overlaid. Data are presented as mean \pm S.E.M. Source data are provided as a Source Data file. © 2025 Allen Institute for Brain Science. Allen Mouse Brain Atlas. Available from: <https://atlas.brain-map.org/>. a was modified from Aime et al., Science 376, 10.1126/science.abk2734 (2022), AAAS.

In vivo electrophysiological recordings

For all the experiments, mice were connected to a tether, digitizing head stage (RHD2132, Intan Technologies), and recordings were done at 20 kHz using an open-source software from Intan Technologies (RHD2000). For the optogenetic experiments additionally to the tetrodes cables, the mice were connected to patch cords coated with black tubing. All the connections within the optic fiber and patch cord, as well as the cement of the implants, were covered by a black varnish in order to reduce the possible excess of light that could disturb the natural sleep of the animals. The experiment started after 10 days, and the auditory stimulation protocol was delivered for 14 sessions after a day of baseline recording. Two sessions have been performed each day, 1 h in the morning and 1 h in the afternoon.

Auditory stimulation

All the experiments were conducted in the same recording room with the same researcher working on them. The mice were in their home cage for the duration of the experiment. All sounds were programmed in MATLAB, where one channel was routed before to the PulsePal system and then to 8 speakers (one speaker per each recorded animal), and the other channel of the PulsePal was routed to the electrophysiology acquisition system. The sounds were played free field through a speaker mounted 30 cm above the animal. For optogenetic experiments, an additional channel was connected from the PulsePal to the lasers, in order to have a precise synchronization of all the outputs. Auditory stimuli included pure tones of 100 ms duration and were interrupted by random gaps of the silence of variable duration (from 1 to 20 s). All the stimuli were presented at three different intensity levels (30-, 55-, and 80-dB SPL) and at three different frequencies (1, 2.5, and 5 kHz).

In vivo optogenetics

For in vivo optogenetic-silencing recording, 2 weeks after viral vector injection, a tetrode was implanted in the CMT (same electrode specifications as in the tetrode implantation section), coupled with a 100- μ m diameter optic fiber mounted 100- μ m above the top electrode contact. Light intensity at optic fiber tips was measured with a power meter (Thorlabs PM100D) before optic fiber insertion (output ≈ 30 mW). We used 532 nm (green light, for optogenetic inhibition) diode laser (Laser Glow). The same protocol mentioned above (in vivo electrophysiological recording) was performed with the difference that the laser was delivered 500 ms before and 500 ms after the auditory stimuli onset.

2-photon laser scanning microscopy

Head-fixed mice were placed and trained under the microscope every day for at least 6 days prior to the experiment, and then longitudinally

imaged using an in vivo 2PLSM (Scientifica HyperScope) equipped with a $\times 16$ objective (0.8 NA, Nikon). ScanImage Software (Vidrio Technologies, LLC) was used to control the microscope, the acquisition parameters, and the TTL-driven synchronization between the acquisition and EEG/EMG recordings. GCaMPs were excited using a Ti: sapphire laser operating at $\lambda = 910$ nm (InSight X3, Spectra-Physics) with an average excitation power at the focal point lower than 50 mW. Time-series images were acquired within a field-of-view of $117 \times 117 \mu\text{m}$ (512×512 pixels). All image analyses were performed using Fiji ImageJ and a custom routine in MATLAB. Each imaging session contained a random presentation of intermingled auditory cues (1 or 5 kHz) during wakefulness or NREM sleep and automatically aligned to the acquired images with a custom-made MATLAB script. No photo-bleaching or photo-toxicity was observed. Acquired images were then corrected by adjusting XY motion artifacts using Suite2p Software⁶³. Regions of interest (ROIs) of cell bodies were selected and drawn manually. All pixels within each ROI were first averaged, providing a single time series of raw fluorescence. Raw calcium traces were then normalized to “F” estimated through a Gaussian distribution-based approach, as previously described⁶⁵. Normalized traces are referred to as “ $\Delta F/F$ ” throughout the paper.

Ca²⁺ event detections. Calcium events were detected using MATLAB custom scripts. Each ROI $\Delta F/F$ trace was analyzed separately after motion correction. Traces were first up-sampled via interpolation to be smoother, with cubic spline interpolation (spline function in Matlab). The baseline median (M) and noise level (E) for each trace are estimated iteratively by computing the median and standard deviation of the signal. Over three iterations, data points exceeding twice the standard deviation are excluded from the subsequent estimation of M and E. Candidate calcium events were identified via the use of the find peaks function in Matlab, using twice the estimated M + E as a threshold for minimum peak height, and M + E as minimum peak prominence.

The characteristics of the candidate events, such as duration, peak amplitude, and integral were computed. Each measured characteristic was then compared with minimum and maximum physiological characteristics, and if not respecting these, excluded. The candidate events were then filtered and confirmed as Ca²⁺ events if their measured characteristics were satisfying some minimum physiological parameters. Physiological parameters used for filtering candidate events were: Minimum Duration of an Event = 1 [s]; Maximum Duration of an Event = 20 [s]; Maximum Ratio between rise and decay duration = 1/3; Minimum Peak Amplitude = 2 [a.u. ($\Delta F/F$)]; Minimum 10 Integral = 1 [a.u. ($\Delta F/F$) \times s]. The measured events were grouped, and an average measure of events per cell, per sleep state (as defined by the sleep hypnogram obtained from the EEGs and EMG scoring), was computed within 15 s of each auditory stimulus presentation.

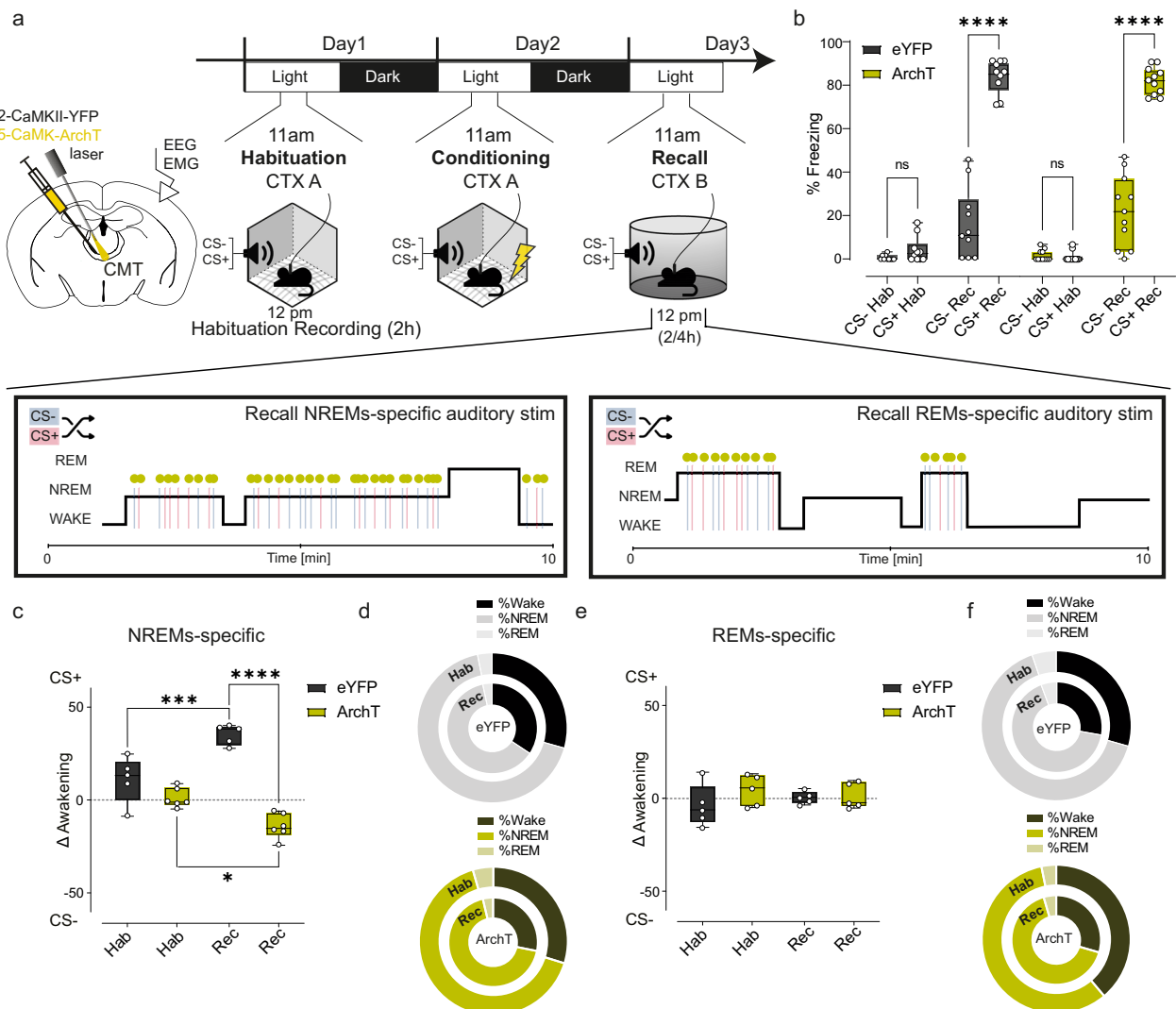


Fig. 6 | Optogenetic silencing of CMT neurons blocks danger vs safety discrimination during NREMs. **a** Experimental schematic showing injection sites and chronic optic fiber implant and EEG/EMG electrodes (left). Right: experimental timeframe including the Habituation, Conditioning, and Recall sessions on separate days and optogenetic silencing window. After memory recall, one group of mice were re-exposed to a randomized sequence (crossed arrows) of CS- and CS+ during NREMs (NREMs-specific auditory stim: eYFP N = 5 mice; ArchT N = 6 mice) and another group of mice during REMs (REMs-specific auditory stim: eYFP N = 5 mice; ArchT N = 5 mice). **b** Percentage of freezing behaviors upon CS- and CS+ exposure during habituation and recall days (N = 21 mice; two-way ANOVA, column factor: $p < 0.0001$, $F(7, 66) = 171.1$; row factor: $p = 0.1041$, $F(10, 66) = 1.680$). **c** Percentage of awakening between the CS- and CS+: Delta values are calculated as the difference between [percentage of awakening for CS+] - [percentage of awakening for CS-] during Habituation (Hab) and Recall (Rec) sessions for the NREM-specific group (two-way ANOVA: interaction $p < 0.0001$, $F(1, 18) = 34.83$; column factor $p < 0.0001$, $F(1, 18) = 78.79$; row factor $p = 0.1833$, $F(1, 18) = 1.915$). **d** Total

percentage duration of wake, NREMs, and REMs in eYFP (N = 5 mice) and in ArchT (N = 6 mice) mice during optogenetic silencing of ArchT-expressing CMT neurons during Habituation and Recall recordings for the NREM-specific group. **e** Same as in (c) but for the REMs-specific group (eYFP N = 5 mice; ArchT N = 5 mice; two-way ANOVA: interaction $p = 0.3104$, $F(1, 16) = 1.098$; column factor $p = 0.2196$, $F(1, 16) = 1.632$; row factor $p = 0.8422$, $F(1, 16) = 0.041$). **f** Same as in (d) but for the REMs-specific group (eYFP N = 5 mice; ArchT N = 5 mice). Data were analyzed using two-way ANOVA with Tukey post hoc test ($*p < 0.05$; $**p < 0.01$; $***p < 0.001$; $****p < 0.0001$). Data were analyzed using two-way ANOVA with Tukey post hoc test or two-sided paired t-tests, as appropriate. Exact p-values, test statistics, and degrees of freedom are reported. Box plots show the median (center line), 25th–75th percentiles (box), and minimum/maximum values (whiskers); individual data points are overlaid. Data are presented as mean \pm S.E.M. Source data are provided as a Source Data file. © 2025 Allen Institute for Brain Science. Allen Mouse Brain Atlas. Available from: <https://atlas.brain-map.org/>.

For population analysis, vectors containing $\Delta F/F$ neuron response amplitude upon auditory stimulation were computed. Pearson correlation analyses were then computed between vectors representing different auditory stimuli (CS- or CS+) at different times (Habituation or Recall) and during different states (Wake or NREM sleep).

Fear conditioning

After a baseline of 2 h per 14 days (same protocol as mentioned before in the section on auditory stimulation), the mice were habituated by gently handling them for 5 min on 5 consecutive days, then on day 28,

the fear conditioning protocol started. On the first day of the procedure (Habituation) at ZTO, a foreign cage with a metal grid as a floor (Context A) was wiped with 70 % ethanol, and the mice were placed in it. The walls were marked with stars to provide additional contextual information. The mice were first given 3 min of time to explore the novel environment, followed by playing a first auditory stimulus (CS-) consisting of 27 pure tones of 100 ms duration at 1 kHz (80 dB SPL) played over 30 s for 5 times with a variable interstimulus interval (ISI) between 10 and 30 s. Then, a second auditory stimulus (CS+) was played under the same conditions but at 5 kHz (80 dB SPL). 24 h later,

the acquisition of fear memories was performed by wiping context A with 70% ethanol again and subsequently placing the animals in the same cage with the metal grid. After 3 min, CS[−] and CS⁺ were played intermixed. An unconditional stimulus (US) was paired with CS⁺ by applying an electric foot shock through the metal grid on the floor at 0.5 mA for 1 s, starting when CS⁺ ended. Another 24 h later (Recall), a novel cage (Context B) was wiped with 1% acetic acid, and mice were placed in it. After 3 min of exploration, CS[−] and CS⁺ were presented to the mice with the same protocol as during habituation. Freezing behavior was measured as a measure of learning performance. It was scored manually as the absence of any movement except breathing. Freezing to CS[−]/CS⁺ was measured during the time the tone was playing, and only the first two rates of CS[−] and CS⁺ were considered. Freezing was quantified as the total time of freezing during the total playing time of the tones. If mice showed generalization by freezing to both CS[−] and CS⁺ during wakefulness on day 3 (Recall), they were excluded from the experiment ($m = 7$ out of 27). The mice that were able to discriminate between the CS[−] and CS⁺ during recall time, underwent the last part of the experiment. Immediately after the cued recall memory test, the mice returned to their home cage, where they were recorded and re-exposed to the safety (CS[−]) and dangerous (CS⁺) sound for 2/4 h while they were sleeping. We tested two different modulations: the first group of mice was exposed to a NREMs-specific auditory stimulation with CMT optogenetic-silencing ($n = 11$), and the second group to REMs-specific auditory stimulation with CMT optogenetic-silencing ($n = 10$).

Data analysis

Pre-processing of LFP data and peaks analysis. Following the acquisition, LFP raw recordings were sampled at 1000 Hz and re-referenced with a common average reference to reduce possible volume conduction. The data were then z-scored. After detecting LFP responses to auditory stimulation, a comprehensive analysis was carried out to examine the timing and amplitude of the peaks, calculating the average of all trials per mouse. The onset of the LFP peak was defined as the first negative peak after the auditory stimulation at 0 ms, corresponding to the early response within the 0 to 50 ms time window. No threshold was applied for this step, as the analysis focused on the distinct negative peak following the auditory stimulation. The second peak, corresponding to the late component of the auditory-evoked response, was analyzed within the 50 to 100 ms time window. For both components, we calculated the latency and amplitude of the detected LFP peaks, representing early and late responses, respectively. These analyses are presented in Supplementary Fig. 2b, c.

Sleep scoring. Sleep scoring was performed manually, based on frequency and amplitude characteristics of the EEG and EMG in custom software written in MATLAB, which allowed for more flexible and accurate scoring based on continuous data rather than segmented epochs. NREMs was identified by high amplitude, synchronous activity in the EEG with a prominent delta (0.5–4 Hz) frequency power, and low EMG activity; REMs was defined by high synchronous theta (6–9 Hz) and flat EMG; wake was characterized by an increase in EMG activity with a low-amplitude, high-frequency (>6 Hz) EEG.

Arousal threshold analysis. Arousals were determined using EMG recordings. In cases where EEG and EMG arousals did not occur simultaneously, we specifically relied on EMG data to identify arousal events. This approach ensured accurate detection of arousal based on muscle activity, even when discrepancies in timing occurred between EEG and EMG signals. We analyzed the averaged LFP activity in response to the stimuli splitting the recording into two groups, based on the behavior of the animals: ^ANREMs-NREMs transitions, are the events in which the animals were not waking up from 0 after 5 s of the auditory stimulations, and ^ANREMs-WAKE transitions are the events in

which the animals were waking up from 0 to 5 s after the auditory stimulation. As previously described in the section “Sleep scoring,” the different states (WAKE, NREMs, and REMs) were defined manually by the EEG/EMG recording.

To assess how the animals were awakening from sleep in response to the different tones used in the fear conditioning protocol (CS[−] and CS⁺), we used a similar analytical approach as described earlier, measuring the events in which the animals woke up within 0–5 s after the stimulation. However, in this case, we calculated the percentage of trials in which the animal woke up in response to each tone (CS[−] or CS⁺), which was obtained by dividing the number of trials in which the animal woke up for the specific tone by the total number of stimulations, i.e., the sum of the number of CS[−] and CS⁺ trials. It is important to mention that the protocol included an equal number of CS[−] and CS⁺ tones. Next, we computed the difference in awakening between the CS[−] and CS⁺ tones by calculating the delta of awakening, which is obtained by subtracting the percentage of awakening in response to the CS[−] tone from the percentage of awakening in response to the CS⁺ tone. This analysis allowed us to determine whether the animals exhibited a differential response to the two tones, as indicated by a higher percentage of awakening for the CS[−] tone compared to the CS⁺ tone.

Slow wave detection. Individual slow waves were detected during NREM sleep using the SWA-MATLAB toolbox⁶⁴, with detection parameters adjusted for rodents based on settings described by Panagiotou et al. and Facchin et al.^{65,66}. The negative envelope of the LFP signal was calculated and filtered between 0.5 and 4 Hz using a Chebyshev Type II filter design. Consecutive zero-crossings were then identified, and slow waves were detected if the duration between the negative-going and subsequent positive-going zero-crossing was between 100 ms and 1 s. The peak negative amplitude of the wave was required to be at least three standard deviations from the median amplitude of all negative peaks in the recording. This amplitude threshold minimized the influence of individual differences in electrode reference type, reference distance, and electrode depth, which could affect the recorded amplitude.

The beginning of each slow wave was marked at the positive-to-negative zero-crossing preceding the negative peak, while the end of the slow wave was defined as the subsequent positive slope's conclusion. In the polar plots, statistical tests are represented by circles numbered with 0.1, 0.2, displayed on the central polar plot. Black lines indicate mean circular vectors. The phase in the plots adheres to the cosine convention, where 0° represents the positive peak (UP state) and 180° marks the peak of the negative slope (DOWN state). Insets provide magnified views of the mean circular vectors within the unit circle.

Spindle detection. Two methods were employed for analyzing spindles. The initial approach involved using the neural network, wherein a filtering range of 9–16 Hz, 10–20 Hz, and then from 10 to 40 Hz was applied to expand the dataset with more values suitable for neural network input. Additionally, a secondary analysis was conducted using a custom-made script, wherein the spindles were detected for each LFP channel and for the EEGs (spindleDetection_pathLoop). We detected spindles using the wavelet method from Wamsley et al. and Bandarabadi et al.^{67,68}. We extracted wavelet energy from the complex frequency B-spline function with the highest normalized power. The wavelet energy time series was smoothed with a 200 ms Hann window, and a threshold of 3 SD above the mean identified potential spindle events, while a lower threshold of 1 SD indicated event starts and ends. Events shorter than 400 ms or longer than 2 s were discarded. Using band-pass-filtered LFP signals in the spindle range (9–16 Hz), we excluded events with fewer than 5 or more than 30 cycles. To ensure wavelet energy increases were spindle-specific, we compared power in

the spindle range with that in 6–8.5 Hz and 16.5–20 Hz, discarding events where spindle power was lower. We estimated spindle central frequency via Fourier transform and assessed symmetry using the peak position of the wavelet energy time series, with values ranging from 0 to 1 (0.5 indicating symmetry). As a first step, the spindle rate was calculated for all the different recordings (14 sessions per animal), then averaged per mouse. Digging more into the analysis we also wanted to analyze the role of spindles in Δ NREMs-to-WAKE transitions, so we plot all the spindles found in events in which the animals were staying in NREMs (Δ NREMs-NREMs) and events in which animals were waking up (Δ NREM-WAKE) before (–5; 0 s) and after (–5; 5 s) the auditory stimulation onset. Then we calculated the percentage of spindles in Δ NREMs-NREMs and Δ NREMs-to-WAKE transitions ($\% = (\text{spindles} / \text{number of transitions}) \times 100$).

Single-unit activity and spike sorting. Single-unit activity was detected using the Offline Sorter Application by Plexon Neurotechnology Research System (version 4.4.1). Raw LFP data were first band-pass filtered (500–4000 Hz, Butterworth filter) and then a threshold for multiunit activity was set manually (depending on the recording from –2 to –6 SD). Single-unit activity was then extracted using principal components analysis and manually extracting clusters. The spike ratio for the PSTH was calculated as the total number of spikes found for each trial, divided per number of events, and averaged for all the animals. For the quantification per animal, there were calculated the number of spikes found during the stimulus onset (from 0 to 0.1 s) divided per event and then averaged per animal.

Burst firing of single units was detected as a minimum of three consecutive action potentials with ISI < 6 ms and preceded by a quiescent hyperpolarized state of at least 60 ms. On the basis of the observed pattern of response, a time window (0–0.1, 0–0.2, 0–0.3, 0–0.4, 0–0.5 s) was selected to analyze the response of a given neuron. For each cell, the values of spontaneous (before the tone) and evoked (during/after the tone) activity obtained during maintained NREM sleep (Δ NREMs-NREMs) were compared with the events with the transition to wake (Δ NREMs-WAKE), using paired t-test.

Decoding and feature extraction with CNNs. A Convolutional Neural Network (CNN), with an EEGNet architecture⁶⁹, was trained to discriminate the conditions Δ NREMs-NREMs vs. Δ NREMs-WAKE based on LFP and EEG traces, extracted from a time interval of 10 s pre- to 5 s post-sound onset, using a tenfold cross-validation scheme. This network has already been successfully used to discriminate electrophysiological responses to auditory stimuli. The network was trained on the raw LFP traces of the HP, CMT, and AU1 as well as the Frontal and Parietal EEG channels. The data of the CMT was filtered in the spindles range (9–16 Hz). Accuracy was computed via the area under the receiver operating characteristic curve (AUC). The trained networks were then used to extract condition-specific activation maps⁷⁰, reflecting the features that were most relevant to the network's decisions, with the use of saliency map, as it is a common practice in the field⁷¹, which were computed at the single-trial level for all correctly classified trials and then averaged over all mice and overall ten trained networks to increase stability, as in previous work⁷¹. EEGNet architecture was used with the standard parameters, as in its original implementation (dropoutRate = 0.5, kernLength = 64, F1 = 8, D = 2, and F2 = 16)⁶⁹. The data were of shape (channels = 5) \times (time points = 15,001) and were given as input to the network in batches of size 32. The network was trained for 50 training iterations with an Adam optimizer⁷² with a learning rate of 0.01, and the rest of the hyperparameters were kept as suggested in the original publication⁶⁹. We trained the network in a 10-fold cross-validation, where the train data split was used for the training of the network, the validation split was used for the evaluation of hyperparameter settings of the network, and the test set was only considered for the overall evaluation of the

network's performance. The train set contained 81% of trials, amounting to 12076 over both classes, the validation set was 10% with a total of 1491 trials, and the test set enclosed 9% of the data summing up to 1342 trials. In the main text, we only report the AUC score for all three sets; however we also additionally evaluated the mean precision, recall, and the F1-score over all ten folds.

Statistical analysis. Data were compared using two-way ANOVA, or t-tests for parametric data, with post hoc Tukey's corrections for multiple comparisons. Post hoc tests were selected based on the comparison type: Sidák was used for pairwise planned comparisons, while Tukey was applied when comparing all group combinations. The assumption of normal distribution was made for parametric tests, but was not formally tested. All values are reported as mean \pm standard error of the mean (S.E.M.), unless otherwise specified. Sample sizes (n) and statistical details for each experiment are provided in the corresponding figure legends.

Histology

Tissue collection. At the end of all experiments, animals were anesthetized with isoflurane as described above, and an electric current was sent through two channels of each tetrode (30 μ A, 5 pulses at 2 s) in order to induce gliosis at the very end of tetrode placement. After ~2 h (time to create an internal scar), mice were euthanized with 15 mg pentobarbital i.p., and the cardiovascular system was transfused with 30 mL of cold, heparinized phosphate-buffered saline (PBS), followed by 30 mL of 4% Paraformaldehyde (PFA) via puncture in the left ventricle of the heart. Brains were removed and kept in PFA at 4 °C overnight, and then they were cryoprotected in 30% sucrose for 48 h. Next, they were flash-frozen in 2-methyl butane at approximately –80 °C, cut into 40 nm thick sections, and stored in PBS at 4 °C. In order to confirm tetrode placement, the tetrodes were stained with 1,1-Dioctadecyl-3,3,3,3-tetramethyl-indocarbocyanine-perchlorate before implantation. After cutting the brain, sections with visible dye traces were selected and either Nissl-stained to reveal the gliosis.

Immunohistochemistry. The viral expression specificity and efficacy were checked histologically by double staining of free-floating sections. The brain sections were washed in PBS 0.1% Triton X-100 (PBST) three times for 10 min each, blocked by incubation with 4% bovine serum albumin dissolved in PBST for 45 min, and subsequently incubated with anti-GFP antibodies (AB_221569, 1:500 dilution in PBST) for 24 h at 4 °C. Then, sections were washed again in PBST (three times for 10 min each) and incubated with a secondary antibody (ab150073, 1:1000 dilution in PBST) that binds to the primary antibody for 1 h at room temperature.

Fluorescence microscopy. Images were acquired by a Nikon Ti-E microscope with a 40 \times resolution. For tetrode placement, a filter Cy3 was used. Instead of fluorescent staining.

Reporting summary

Further information on research design is available in the Nature Portfolio Reporting Summary linked to this article.

Data availability

All raw data used for analysis are made available through the Supplementary Information. Source data are provided as a Source Data file. Source data are provided with this paper.

Code availability

All scripts used for analysis are available through a GitHub repository (<https://github.com/ZENLabCode>). The code is available at: <https://doi.org/10.5281/zenodo.15467591>.

References

- Colrain, I. M. & Campbell, K. B. The use of evoked potentials in sleep research. *Sleep. Med. Rev.* **11**, 277–293 (2007).
- Andrillon, T. & Kouider, S. The vigilant sleeper: neural mechanisms of sensory (de)coupling during sleep. *Curr. Opin. Physiol.* **15**, 47–59 (2020).
- Dang-Vu, T. T. et al. Interplay between spontaneous and induced brain activity during human non-rapid eye movement sleep. *Proc. Natl. Acad. Sci. USA* **108**, 15438–15443 (2011).
- Schabus, M. et al. The fate of incoming stimuli during NREM sleep is determined by spindles and the phase of the slow oscillation. *Front. Neurol.* **3**, 40 (2012).
- Edeline, J. M., Manunta, Y. & Hennevin, E. Auditory thalamus neurons during sleep: changes in frequency selectivity, threshold, and receptive field size. *J. Neurophysiol.* **84**, 934–952 (2000).
- Simor, P., van der Wijk, G., Nobili, L. & Peigneux, P. The microstructure of rapid eye movement (REM) sleep: Why phasic and tonic? *Sleep Med. Rev.* **52**, 101305 (2020).
- Nir, Y., Vyazovskiy, V. V., Cirelli, C., Banks, M. I. & Tononi, G. Auditory responses and stimulus-specific adaptation in rat auditory cortex are preserved across non-rapid eye movement (NREM) and rapid eye movement (REM) sleep. *Cereb. Cortex* **25**, 1362–1378 (2015).
- Züst, M. A., Ruch, S., Wiest, R. & Henke, K. Implicit vocabulary learning during sleep is bound to slow-wave peaks. *Curr. Biol.* **29**, 541–553.e7 (2019).
- Ibáñez, A., López, V. & Cornejo, C. Event-related potentials (ERPs) and contextual semantic discrimination: degrees of congruence in wakefulness and sleep. *Brain Lang.* **98**, 264–275 (2006).
- Lee, C. C. & Murray Sherman, S. Drivers and modulators in the central auditory pathways. *Front. Neurosci.* **4**, 79–86 (2010).
- Wang, Y. et al. A common thalamic hub for general and defensive arousal control. *Neuron* **111**, 3270–3287.e8 (2023).
- Edeline, J. M., Dutrieux, G., Manunta, Y. & Hennevin, E. Diversity of receptive field changes in auditory cortex during natural sleep. *Eur. J. Neurosci.* **14**, 1865–1880 (2001).
- Cusinato, R. et al. Intrinsic neural timescales in the temporal lobe support an auditory processing hierarchy. *J. Neurosci.* **43**, 3696–3707 (2023).
- Hayat, H. et al. Locus coeruleus norepinephrine activity mediates sensory-evoked awakenings from sleep. *Sci. Adv.* **6**, eaz4232 (2020).
- Shin, A. et al. A brainstem-to-mediadorsal thalamic pathway mediates sound-induced arousal from slow-wave sleep. *Curr. Biol.* **33**, 875–885 (2023).
- Gent, T. C., Bandarabadi, M., Herrera, C. G. & Adamantidis, A. R. Thalamic dual control of sleep and wakefulness. *Nat. Neurosci.* **21**, 974–984 (2018).
- Gent, T. C., Bassetti, C. L. A. & Adamantidis, A. R. Sleep-wake control and the thalamus. *Curr. Opin. Neurobiol.* **52**, 188–197 (2018).
- Lecci, S. et al. Coordinated infraslow neural and cardiac oscillations mark fragility and offline periods in mammalian sleep. *Sci. Adv.* **3**, e1602026 (2017).
- Gottesmann, C. The transition from slow-wave sleep to paradoxical sleep: evolving facts and concepts of the neurophysiological processes underlying the intermediate stage of sleep. *Neurosci. Biobehav. Rev.* **20**, 367–387 (1996).
- van Kronenberg, P., Milinski, L., Kruschke, Z. & de Hoz, L. Sound disrupts sleep-associated brain oscillations in rodents in a meaning-dependent manner. *Sci. Rep.* **12**, 1 (2022).
- Portas, C. M. et al. Auditory processing across the sleep-wake cycle: simultaneous electroencephalogram and functional magnetic resonance imaging monitoring in humans. *Brain* **123**, 821–828 (2000).
- Oswald, I., Taylor, A. M. & Treisman, M. Discriminative responses to stimulation during human sleep. *Brain* **83**, 440–453 (1960).
- Poitras, R., Thorkildsen, A., Gagnon, M. A. & Naiman, J. Auditory discrimination during rapid eye movement (REM) and non-rapid eye movement (NREM) sleep in women before and after delivery. *Electroencephalogr. Clin. Neurophysiol.* **35**, 603–609 (1973).
- Bastuji, H., Perrin, F. & Garcia-Larrea, L. Semantic analysis of auditory input during sleep: studies with event-related potentials. *Clin. Neurophysiol.* **113**, 1906–1916 (2002).
- Ledoux, J. E., Sakaguchi, A. & Reis, D. J. Subcortical efferent projections of the medial geniculate nucleus mediate emotional responses conditioned to acoustic stimuli. *J. Neurosci.* **3**, 613–624 (1983).
- Mátyás, F. et al. A highly collateralized thalamic cell type with arousal-predicting activity serves as a key hub for graded state transitions in the forebrain. *Nat. Neurosci.* **21**, 1551–1562 (2018).
- Van Der Werf, Y. D., Witter, M. P. & Groenewegen, H. J. The intralaminar and midline nuclei of the thalamus: anatomical and functional evidence for participation in processes of arousal and awareness. *Brain Res. Rev.* **39**, 107–140 (2002).
- Hermann, D. M. et al. Evolution of neurological, neuropsychological and sleep-wake disturbances after paramedian thalamic stroke. *Stroke* **39**, 62–68 (2008).
- Otake, K., Kin, K. & Nakamura, Y. Fos expression in afferents to the rat midline thalamus following immobilization stress. *Neurosci. Res.* **44**, 157–170 (2002).
- Penzo, M. A. et al. The paraventricular thalamus controls a central amygdala fear circuit. *Nature* **519**, 455–459 (2015).
- Do-Monte, F. H., Quiñones-Laracuente, K. & Quirk, G. J. A temporal shift in the circuits mediating retrieval of fear memory. *Nature* **519**, 460–463 (2015).
- Lee, S. et al. Bidirectional modulation of fear extinction by medio-dorsal thalamic firing in mice. *Nat. Neurosci.* **15**, 308–314 (2011).
- Cash, S. S. et al. The human K-complex represents an isolated cortical down-state. *Science* **324**, 1084–1087 (2009).
- Mak-McCully, R. A. et al. Synchronization of isolated downstates (K-complexes) may be caused by cortically-induced disruption of thalamic spindling. *PLoS Comput. Biol.* **10**, e1003855 (2014).
- Bastuji, H., Lamouroux, P., Villalba, M., Magnin, M. & Garcia-Larrea, L. Local sleep spindles in the human thalamus. *J. Physiol.* **598**, 2109–2124 (2020).
- Sherman, S. M. A wake-up call from the thalamus. *Nat. Neurosci.* **4**, 344–346 (2001).
- Antonini, A. et al. Extended field-of-view ultrathin microendoscopes for high-resolution two-photon imaging with minimal invasiveness. *eLife* **9**, e58882 (2020).
- Loftus, J. C., Harel, R., Núñez, C. L. & Crofoot, M. C. Ecological and social pressures interfere with homeostatic sleep regulation in the wild. *eLife* **11**, e77409 (2022).
- Lima, S. L., Rattenborg, N. C., Lesku, J. A. & Amlaner, C. J. Sleeping under the risk of predation. *Anim. Behav.* **70**, 723–736 (2005).
- Amlaner, C. J. & Rattenborg, N. *The Evolution of Sleep* (Sleep Research Society, 2009).
- Rattenborg, N. C., Lima, S. L. & Amlaner, C. J. Facultative control of avian unihemispheric sleep under the risk of predation. *Brain Behav. Evol.* **105**, 62–67 (1999).
- Fernandez, L. M. J. & Lüthi, A. Sleep spindles: mechanisms and functions. *Physiol. Rev.* **100**, 805–868 (2020).
- Tseng, Y. T. et al. The subthalamic corticotropin-releasing hormone neurons mediate adaptive REM-sleep responses to threat. *Neuron* **110**, 1223–1239.e8 (2022).
- Tasserie, J. et al. Deep brain stimulation of the thalamus restores signatures of consciousness in a nonhuman primate model. *Sci. Transl. Med.* **8**, eabc1234 (2022).
- McKenna, J. T. et al. Basal forebrain parvalbumin neurons mediate arousals from sleep induced by hypercarbia or auditory stimuli. *Curr. Biol.* **30**, 2379–2385.e4 (2020).

46. Massaux, A., Dutrieux, G., Cotillon-Williams, N., Manunta, Y. & Edeline, J. M. Auditory thalamus bursts in anesthetized and non-anesthetized states: contribution to functional properties. *J. Neurophysiol.* **91**, 2117–2134 (2004).
47. Schmitt, L. I. et al. Thalamic amplification of cortical connectivity sustains attentional control. *Nature* **545**, 219–223 (2017).
48. Padilla-Coreano, N., Do-Monte, F. H. & Quirk, G. J. A time-dependent role of midline thalamic nuclei in the retrieval of fear memory. *Neuropharmacology* **62**, 457–463 (2012).
49. Guido, W. & Weyand, T. Burst responses in thalamic relay cells of the awake behaving cat. *J. Neurophysiol.* **74**, 1782–1793 (1995).
50. Vertes, R. P., Hoover, W. B. & Rodriguez, J. J. Projections of the central medial nucleus of the thalamus in the rat: Node in cortical, striatal and limbic forebrain circuitry. *Neuroscience* **219**, 120–136 (2012).
51. Vertes, R. P., Linley, S. B. & Rojas, A. K. P. Structural and functional organization of the midline and intralaminar nuclei of the thalamus. *J. Comp. Neurol.* **530**, 336–357 (2022).
52. Halperin, J. M. & Iorio, L. C. Responsivity of rats to neutral and danger-signaling stimuli during sleep. *Behav. Neural Biol.* **33**, 213–219 (1981).
53. Snyder, F. Toward an evolutionary theory of dreaming. *Am. J. Psychiatry* **123**, 121–136 (1966).
54. Rechtschaffen, A., Hauri, P. & Zeitlin, M. Auditory awakening thresholds in REM and NREM sleep stages. *Percept. Mot. Skills* **22**, 927–942 (1966).
55. Hellman, K. & Abel, T. Fear conditioning increases NREM sleep. *Behav. Neurosci.* **121**, 310–323 (2007).
56. LeDoux, J. E., Cicchetti, P., Xagoraris, A. & Romanski, L. M. The lateral amygdaloid nucleus: sensory interface in fear conditioning. *J. Neurosci.* **10**, 1062–1069 (1990).
57. Schreck, M. R. et al. State-dependent olfactory processing in freely behaving mice. *Cell Rep.* **38**, 110450 (2022).
58. Schott, A. L., Baik, J., Chung, S. & Weber, F. A medullary hub for controlling REM sleep and pontine waves. *Nat. Commun.* **14**, 3933 (2023).
59. Osorio-Forero, A. et al. Noradrenergic circuit control of non-REM sleep substates. *Curr. Biol.* **31**, 5009–5023.e7 (2021).
60. Lyamin, O. I., Mukhametov, L. M. & Siegel, J. M. Sleep in the northern fur seal. *Cur. Opin. Neurobiol.* **44**, 133–151 (2017).
61. Rattenborg, N. C. Somnolism. *Sleep. Med.* **67**, 246–247 (2020).
62. Beauchamp, G. Sleeping gulls monitor the vigilance behaviour of their neighbours. *Biol. Lett.* **5**, 9–11 (2009).
63. Aime, M. et al. Paradoxical somatodendritic decoupling supports cortical plasticity during REM sleep. *Science* **376**, 724–730 (2022).
64. Mensen, A., Riedner, B. & Tononi, G. Optimizing detection and analysis of slow waves in sleep EEG. *J. Neurosci. Methods* **274**, 1–12 (2016).
65. Facchin, L. et al. Slow waves promote sleep-dependent plasticity and functional recovery after stroke. *J. Neurosci.* **40**, 8637–8651 (2020).
66. Panagiotou, M., Vyazovskiy, V. V., Meijer, J. H. & Deboer, T. Differences in electroencephalographic non-rapid-eye movement sleep slow-wave characteristics between young and old mice. *Sci. Rep.* **7**, 43656 (2017).
67. Wamsley, E. J. et al. Reduced sleep spindles and spindle coherence in schizophrenia: mechanisms of impaired memory consolidation. *Biol. Psychiatry* **71**, 154–161 (2012).
68. Bandarabadi, M. et al. A role for spindles in the onset of rapid eye movement sleep. *Nat. Commun.* **11**, 5247 (2020).
69. Lawhern, V. J. et al. EEGNet: A compact convolutional neural network for EEG-based brain–computer interfaces. *J. Neural Eng.* **15**, 056013 (2018).
70. Simonyan, K., Vedaldi, A. & Zisserman, A. Deep inside convolutional networks: visualising image classification models and saliency maps. Preprint at <https://arxiv.org/abs/1312.6034> (2013).
71. Aellen, F.M. et al. Convolutional neural networks for decoding electroencephalography responses and visualizing trial by trial changes in discriminant features. *J. Neurosci. Methods* **364**, 109367 (2021).
72. Kingma, D. P. & Ba, J. Adam: A method for stochastic optimization. Preprint at <https://arxiv.org/abs/1412.6980> (2014).

Acknowledgements

We thank all the Tidis Lab members for their insightful discussion of, and comments on, previous versions of the manuscript. This work was supported by the Inselspital University Hospital Bern, and Interfaculty Research Cooperation (A.A., A.T. and C.G.H.), Swiss National Science Foundation (A.A.), the University of Bern (A.A.), European Research Council (A.A.), Synapsis Foundation (A.A.) and the EU H2020-ICT grant (A.S. and T.F.).

Author contributions

I.L.B., M.A., and C.G.H. performed the experiments. F.A., with the supervision of A.Z., trained the neural network and performed the computational approach analysis. I.L.B., F.A., A.T., T.R., M.A., I.B., and M.B. analyzed the data. I.L.B. and A.A. conceived the studies and wrote the manuscript with the help of all the authors. A.A. supervised the research. A.S. and T.F. provided technical assistance with the fabrication of aberration-corrected endoscopes.

Competing interests

The authors declare no competing interests.

Additional information

Supplementary information The online version contains supplementary material available at <https://doi.org/10.1038/s41467-025-62265-0>.

Correspondence and requests for materials should be addressed to Antoine Adamantidis.

Peer review information *Nature Communications* thanks Anna Shin and the other, anonymous, reviewer(s) for their contribution to the peer review of this work. A peer review file is available.

Reprints and permissions information is available at <http://www.nature.com/reprints>

Publisher's note Springer Nature remains neutral with regard to jurisdictional claims in published maps and institutional affiliations.

Open Access This article is licensed under a Creative Commons Attribution-NonCommercial-NoDerivatives 4.0 International License, which permits any non-commercial use, sharing, distribution and reproduction in any medium or format, as long as you give appropriate credit to the original author(s) and the source, provide a link to the Creative Commons licence, and indicate if you modified the licensed material. You do not have permission under this licence to share adapted material derived from this article or parts of it. The images or other third party material in this article are included in the article's Creative Commons licence, unless indicated otherwise in a credit line to the material. If material is not included in the article's Creative Commons licence and your intended use is not permitted by statutory regulation or exceeds the permitted use, you will need to obtain permission directly from the copyright holder. To view a copy of this licence, visit <http://creativecommons.org/licenses/by-nc-nd/4.0/>.

© The Author(s) 2025